Eruption frequency and magnitude in a geothermally active continental rift: The Bora-Baricha-Tullu Moye volcanic complex, Main Ethiopian Rift

A.Z. Tadesse[1*], K. Fontijn[1,2], A.A. Melaku[3], E.F. Gebru[3,4], V.C. Smith[5], E. Tomlinson[6], D. Barfod[7], P. Gopon[2,8], F. Bégué[9], L. Caricchi[9], P. Laha[10], H. Terryn[10], S. Gudbrandsson[11], G. Yirgu[3], D. Ayalew[3]

[1]Department of Geosciences, Environment and Society, Université libre de Bruxelles (ULB), Belgium.

[2]Department of Earth Sciences, University of Oxford, UK.

[3]School of Earth Sciences, Addis Ababa University (AAU), Ethiopia.

[4]Department of Geosciences, Université de Fribourg (UNIFR), Switzerland.

[5]Research Laboratory for Archaeology and the History of Art, University of Oxford, UK.

[6]Department of Geology, Trinity College Dublin (TCD), Ireland.

[7]NEIF Argon Isotopes, Scottish Universities Environmental Research Centre, UK.

[8]Department of Applied Geosciences and Geophysics, University of Leoben, Austria.

[9]Department of Earth Sciences, University of Geneva (UNIGE), Switzerland.

[10]Research Group of Electrochemical and Surface Engineering, Department of Materials and Chemistry, Vrije Universiteit Brussel (VUB), Belgium.

[11]Reykjavik Geothermal Ltd, Iceland.

*Corresponding author: Amdemichael.Tadesse@ulb.be, amdemichaelz@gmail.com, Tel +32471309363

Abstract

Many Quaternary silicic volcanoes in the Main Ethiopian Rift pose a potential risk due to the poorly known eruptive histories of the volcanoes in combination with a high population density. In this study we provide new constraints on the Late Pleistocene-Holocene eruptive history of the Bora-Baricha-Tullu Moye (BBTM) volcanic complex located in the central portion of the Main Ethiopian Rift (MER). BBTM constitutes three main silicic edifices (i.e. Bora, Baricha and Tullu Moye) and numerous smaller vents (including Oda and Werdi). Tephra deposits from these vents are several centimetres to meters in thickness in currently densely populated regions and where geothermal development is taking place. We present new field observations in addition to physical, petrographic, geochemical and geochronological data. BBTM experienced at least 27 explosive eruptions, of varying magnitude, in the last ca. 100 ky. The two oldest tephra deposits in our compiled stratigraphy are associated with large-magnitude, and possibly caldera-forming eruptions. The youngest of these (Meki) occurred at 107.7 ± 8.8 (2σ) ka, which makes it the youngest caldera-forming eruption identified in the Central MER so far. During the post-caldera stage, BBTM underwent at least 25 eruptions sourced from the Baricha (9 eruptions), Bora (3), Oda (8), Werdi (3) and Tullu Moye (2) edifices. The return period of explosive activity in BBTM is thus at least one moderate-to-large explosive eruption every 4000 yr. Well-exposed units have estimated eruption magnitudes (M) that are 4 to 5, while smaller-scale eruptions reach up to 2.5 and are exclusively preserved near the Tullu Moye vent. The tephra was dispersed up to 20 km from the volcanic complex suggesting that more than one hundred thousand

people could be exposed to tephra fall and pyroclastic density current hazards from future of similar-magnitude eruptions in this area.

Key words

Bora-Baricha-Tullu Moye; Main Ethiopian Rift; tephrostratigraphy; explosive eruptions

1. Introduction

The Main Ethiopian Rift (MER) is a mature volcano-tectonic rift zone with Quaternary silicic volcanoes arranged regularly along the rift axis, and numerous small, fault-controlled mafic eruptive centres (Fig. 1). The silicic volcanoes have produced hundreds of cubic kilometres of highly evolved magmas, and many of them host large caldera depressions and geologically young (i.e. Late Pleistocene-Holocene) edifices formed in the post-caldera stage (e.g. Corbetti: Rapprich et al. 2016; Aluto: Hutchison et al. 2016a, b; and Gedemsa: Peccerillo et al. 2003; Fig. 1). Many of these volcanoes pose a high-risk due to the high population density and their poorly known eruptive histories (Aspinall et al. 2011; Loughlin et al. 2015). Long repose periods (several 100 to 1000 years for some MER volcanoes; Martin-Jones et al. 2017; Fontijn et al. 2018; McNamara et al. 2018; Siegburg et al. 2018) further compromise hazard awareness and, thus, efforts to reduce or mitigate the risk (e.g. Donovan & Oppenheimer 2012). Several MER volcanoes currently show signs of geophysical unrest, primarily in the form of ground deformation detected by satellite radar interferometry (Biggs et al. 2011; Hutchison et al. 2016c; Albino & Biggs 2021). The current study focuses on one of these volcanoes (Bora-Baricha-Tullu Moye) with the aim to improve our understanding of its eruptive history and the related hazard for neighbouring populations and socio-economic development.

The Bora-Baricha-Tullu Moye (BBTM) volcanic complex is located in the central portion of the MER (Fig. 1). Bora, Baricha and Tullu Moye are the three main silicic edifices, among several smaller ones (including Oda and Werdi, Fig. 2). At present BBTM is active and has experienced ongoing low frequency seismicity (e.g. Greenfield et al. 2019 a, b) and episodic ground deformation over at least the past decade (Biggs et al. 2011; Albino & Biggs 2021).

The earliest reconnaissance studies on the distribution of the volcanic products were performed in the 1970s (Di Paola 1972; Bizouard & Di Paola 1978) and recognised that Tullu Moye (in the east of the complex) mainly erupts comendites, and pantellerites are mainly found in the west, around Bora and Baricha. Since then, several studies have focused on the geothermal potential of the area that is 500 MWe annually (UNDP 1973; ELC 1987; Mamo 2002; Varet & Birba 2018). At the time of writing, the area is at an advanced geothermal exploration stage, with ongoing drilling operations that are mainly located on the eastern side (Tullu Moye) of the complex. The location of this significant investment project and the high population density of the area located in towns such as Meki, Alem Tena, Iteya and Assela, all within 20 km of at least one of the main volcanic edifices, motivated this volcanological study.

BBTM experienced several explosive eruptions in the past as identified from a preliminary stratigraphic sequence presented by Fontijn et al. (2018). This study builds on their previous work, providing new field observations, physical (componentry), petrographic, geochemical (glass major and trace element geochemistry), and geochronological ($^{40}Ar/^{39}Ar$ and ^{14}C) data on pyroclastic deposits across the BBTM. We establish a tephrostratigraphic framework for the BBTM volcanic field to constrain the frequency-magnitude relationship of the eruptive events at this active caldera system.

2. Geological Setting

The MER is an active rift zone stretching between the Afar and Turkana depressions in the East African Rift (EAR). The MER is bounded by roughly NE-SW oriented border faults separating the surrounding Eastern and Western Plateaux. The rift gradually narrows from the southern Afar depression into the MER with a minimum width of ~80 km. The southern MER boundary is considered to be located at ~5°N latitude (Balestrieri et al. 2016) where a ~300 km-wide system of basins and ranges called the Broadly Rifted Zone exists (Ebinger et al. 2000). Here, the rift zone widens and the deformation becomes more distributed.

The present-day configuration of the MER suggests the progressive narrowing of volcano-tectonic activity with time that will eventually lead to continental breakup and subsequent oceanic spreading (e.g. Ebinger & Casey 2001; Ebinger 2005; Rooney et al. 2007; Daly et al. 2008; Bastow et al. 2011). The Quaternary deformation and volcanism have mainly concentrated on the axial magmatic segments that are located along a 20 x 60 km zone (i.e. Wonji Fault Belt, WFB; Ebinger & Casey 2001; Keir et al. 2006). In these magmatic segments the younger products erupted from volcanic fissures, scoria cones and large central volcanoes are collectively known as the Wonji group (e.g. WoldeGabriel et al. 1990). This group is dominated by silicic volcanic rocks erupted from the large central volcanoes aligned along the axial zone of the MER (i.e. Corbetti, Aluto, BBTM, Gedemsa, Boku, Boset-Bericha, Kone and Fentale; Fig. 1). These volcanoes are systematically spaced (ca. 20-45 km apart), with edifices rising hundreds of meters above the MER plain. Some of these large silicic edifices are associated with well-developed caldera structures (e.g. Kone, Gedemsa), where others have calderas that are largely concealed by post-caldera eruptive products (e.g. Aluto). The post-caldera eruptive products primarily occur as silicic tephra deposits and (obsidian) lava flows (e.g. Peccerillo et al. 2003; Hutchison et al. 2016a, b; Rapprich et al. 2016; Fontijn et al. 2018).

Volcanic products from the present-day BBTM volcanic centres, including Bora, Baricha and Tullu Moye, overlie Late Pleistocene ignimbrites that have been K-Ar dated to 1.58 ± 0.2 Ma (Table 1; WoldeGabriel et al. 1990). Three borehole wells (TG-1, TG-2 and TG-3; Fig 2) show that the BBTM subsurface geology consists of trachyte and rhyolite lava flows at the base, which are overlain by weakly to moderately compacted layers of ignimbrites and unwelded pyroclastics (Ayele et al. 2002). The rhyolite lavas thin out and the fine-grained ignimbrites become very thick (87.5 m) at TG-2. Another well (TG-4) drilled near a rhyolite dome (Adano) shows very thick (100 m) trachytic and rhyolitic lavas with variable porphyritic to fully glassy (obsidian) texture overlaying an ignimbrite similar to that observed in the rift escarpment (Ayele et al. 2002). Well TG-5 is located close to Tullu Moye volcano and incorporates very thick (90.5 m) porphyritic and scoriaceous basalt at the base. The subsurface lithologies show alteration that is likely related to the persistent hydrothermal activity in the region (Ayele et al. 2002).

The surface geology of Bora and Baricha is characterized by poorly to completely unwelded pumice and ash deposits (Di Paola 1972). Subordinate rhyolitic lavas are associated with the pyroclastics at Baricha (e.g. Di Paola 1972; ELC 1987; Ayele et al. 2002). Near Baricha, Fontijn et al. (2018) identified >7 pantelleritic pumice fall deposits alternating with poorly-developed palaeosols. Several smaller pumice vents are located to the east of Bora and Baricha, including Werdi and Oda (Fig. 2).

Tullu Moye is situated in the intensely faulted part of the region (also known as the Salen range; Varet & Briba 2018) along the WFB, and has trachytic lavas and hydrothermally altered pyroclastic deposits. The whole rock (Bizouard & Di Paola 1978) and glass (Fontijn et al. 2018) chemical compositions indicate that Tullu Moye pumice and obsidian lava have a comenditic composition. The plain located to the NE and SW of Tullu Moye is covered by thick obsidian (at Giano and Janno/Miesa; Ayele et al. 2002) and basaltic flows and associated scoria, spatter and cinder cones. Those products erupted along fissures and conceal some of the earlier Tullu Moye tephra deposits (UNDP 1973; ELC 1987). The Giano obsidian flow (after Bizouard & Di Paola 1978) possibly erupted during historical time (ca. 1900 CE) and covers a 2.7 X 1.6 km area; though detailed accounts of the eruption or its exact age are not known (Gouin 1979).

Since the Late Cenozoic, tectonic activity in the MER caused subsidence and formed an asymmetric basin with fluvio-lacustrine sedimentation (e.g. Le Turdu et al. 1999). Today several lakes exist in this asymmetric MER floor (Fig. 1). Most of these lakes were repeatedly connected and disconnected in the Quaternary as a result of tectonic subsidence and/or lake level fluctuations (Benvenuti et al. 2002, 2013). At least two major lake expansion phases are recorded in the sediments (Benvenuti et al. 2002). The oldest “Megalake” phase occurred around the Late Pleistocene (ca. 100 ka) and is separated from a second lake level high-stand (“macrolake” phase, ca. 10 ka) by an erosional contact that resulted from prolonged low-stand and lake level fluctuations (e.g. Benvenuti et al., 2002; Le Turdu et al. 1999). The fluvio-lacustrine sediments are interbedded with volcanic (pyroclastic and epiclastic) deposits, providing evidence for episodic volcanic activity throughout the Late Quaternary (Le Turdu et al. 1999; McNamara et al. 2018). In the northern and central portions of the MER these lacustrine sediments reach up to tens of meters of thickness (Le Turdu et al. 1999; Benvenuti et al. 2002). Subsurface geophysical investigations (e.g. Mulugeta et al. 2021) and deep boreholes (e.g. Teklemariam et al. 1996) around Aluto volcanic complex reveal lacustrine deposits that are up to 600 m in thickness.

3. Methods

Field campaigns were performed in 2015, 2017 and 2020. A total of 162 outcrops were systematically logged, and samples were collected for each stratigraphic unit from multiple sites around the volcanic complex (Fig. 2a). Pyroclastic units were correlated using a combination of field observations (including lateral tracing between outcrops), physical characteristics and chemical compositions.

Componentry analysis was performed to quantify the proportions of different particle types that occur in tephra deposits sourced from different centres across the BBTM. Eighty-five samples, each up to 2 kg, from selected tephra layers, and in some cases from different stratigraphic levels of the same deposit (e.g. base, middle and top) were dry-sieved at 1ϕ intervals between -2ϕ (4 mm) and 2ϕ (0.25 mm). In each grain size fraction particles were qualitatively assigned into classes, counted and weighed. The assigned classes are: (1) Vesicular juvenile, which are unaltered to slightly altered pumiceous clasts; (2) Dense juvenile, which are poorly- to- non-vesiculated, dense and fresh volcanic glass shards; (3) Accidental dense lithics; and (4) Free crystals, which may be juvenile or xenocrystic. Each class was described qualitatively according to colour, vesicularity, vesicle size, vesicle shape, crystallinity and type (Houghton & Wilson 1989; Cas et al. 2008). Vesicular juvenile clasts of each bed-set were qualitatively described and classified based on colour (i.e. yellow-brown, dark-grey, light grey, bluish-grey and white) and clast textures using nomenclature as per Polacci et al. (2003): expanded (extensive vesicle expansion with >90% interconnected vesicles), microvesicular (equidimensional clasts containing heterogeneous vesicles) and tube (fairly elongated to highly stretched vesicles). The lithic fragments were qualitatively described according to their levels of alteration (i.e. reddish to light brown colour) and nature (lava, obsidian and green ignimbrite). The data presented in section 4.1 is the average of all analysed grain size fractions between 4 mm and 0.25 mm (see Table 2).

Thin sections of selected pyroclastic and lava samples were prepared by TS Lab and Geoservices, Italy. Modal mineral percentages were estimated by an automated point counting method using ImageJ (Schneider et al. 2012) and the image analysis toolbox Jmicrovision 1.3.1 (Roduit 2019). At least 300 points were counted per field-of-view. To measure the areas of vesicles and solid material (groundmass (typically glassy) and crystals), each phase was segmented by manual bi-level greyscale thresholding based on the histogram of the image. Vesicle and groundmass / crystal proportions were then recalculated using the mineral area proportions in the solid phase as obtained from the point counting.

For glass chemical analysis pumice lapilli were manually crushed using an agate pestle and mortar. The crushed samples were wet-sieved at 80 µm to remove the finer clay-sized fraction that cannot be analysed and dried in an oven at 50 $^{\circ}$C. The recovered fresh shards were cold-mounted in pre-drilled EpoFix resin discs and polished with SiC paper (grade P1200 and P2400) and diamond paste (3 and 1 micron). Back-scattered electron (BSE) imaging and semi-quantitative compositional analyses were performed with a JEOL JSM-IT300 scanning electron microscope fitted with an Oxford instruments SDD X-MaxN EDS detector at the Department of Materials and Chemistry, Vrije Universiteit Brussel (VUB) to determine suitable points for qualitative glass analysis, avoiding phenocrysts and microlites. The SEM and EDS data for selected samples is displayed in the supplementary material (SM-1).

Glass major element data was acquired by Electron Microprobe Analysis (EPMA) using a JEOL JXA-8600 Superprobe (Research Laboratory for Archaeology and the History of Art, University of Oxford), a JEOL 8200 (Department of Earth Sciences, University of Geneva) and a CAMECA SX5-FE (Department of Earth Sciences, University of Oxford). On all three instruments, the same analytical protocol was used. Analyses were conducted on carbon-coated polished grain mounts using an accelerating voltage of 15 kV, a low beam current (6 nA) and a defocused beam of 10 µm. For samples with smaller glass areas, a 4 nA beam current and a probe diameter of 6 µm were used. Counting times on the peak were set to 30 seconds (Si, Al, Ti, Ca) and 60 seconds (P, Mg, Mn, Fe). Due to Na and K mobility and loss issues, Na and K were analysed first on each spectrometer, and were measured with a short peak count time of 12 seconds. The background count times at the high and low background where half of the peak count time. The instruments were calibrated with a suite of appropriate mineral standards, listed on supplementary material (SM-2). Analysis of secondary glass standards (ATHO-G, StHs6/80-G and MLB-3-G; Jochum et al. 2006) was used to regularly verify the calibration. The secondary standards analytical precision is typically < ± 4% relative standard deviation (RSD) for most major elements, except for the low abundance elements such as Ti (± 8%), Mn (± 30%) and P (± 38%). At least 20 individual points were analysed per sample. Only analyses with totals above 92 wt% were considered reliable, and data were normalized to 100% before being plotted (Frogatt 1983; Lowe 2011). A representative set of analyses are presented in Table 3; the full data set is available in supplementary material (SM-2).

Trace element analyses of glass shards for some tephra units were conducted by Laser Ablation – Inductively Coupled Plasma – Mass Spectrometry (LA-ICP-MS) at the iCRAG laboratory, Trinity College Dublin (TCD) using a Teledyne Photon Machine G2 193 nm excimer laser ablation system with a two-volume Helex cell coupled to a Thermo Scientific iCAPQ ICP-MS. We used a spot size of 30 μm, a repetition rate of 5 Hz with a 35 s acquisition time with 30 s for washout between samples. Concentrations were calibrated using a NIST612 glass standard (using the composition reported by Jochum et al. 2011) with ^{29}Si as the internal standard. During the measurement, the calibration was verified using MPI-DING glasses (ATHO-G and StHs6/80-G; Jochum et al. 2006). Data reduction was undertaken using Iolite 3.4. The secondary standards trace element analysis precision is typically ≤11% except for Rb, Sr, Y and Nb (≤7%) in RSD.

Two pumice samples (MER149A and MER147-2D) were prepared at the Department of Earth Sciences, University of Oxford for single-crystal $^{40}Ar/^{39}Ar$ dating. The samples were crushed and sieved, and 250-500 μm size fractions were recovered. These fractions were cleaned in distilled water in an ultrasonic bath, dried in an oven at 50 °C and passed multiple times through a Frantz Isodynamic magnetic separator to concentrate sanidine crystals. The sanidine concentrates were leached in 5% HF to remove any adhering glass, and examined under a binocular microscope to collect pristine, inclusion-free, grains. Dating was performed at the NEIF Argon Isotope Laboratory at the Scottish Universities Environment Research Centre (SUERC), University of Glasgow. Samples and neutron flux monitors were packaged in aluminium discs and stacked in quartz tubes for later reconstruction of neutron flux gradients. The sample package was irradiated in the Oregon State University reactor, Cd-shielded facility. Alder Creek sanidine (1.1891 ± 0.0008 (1σ) Ma; Niespolo et al. 2017) was used to monitor ^{39}Ar production and establish neutron flux values (J) for samples. Ar isotopic measurement was performed on a MAP-215-50 instrument, single-collector mass spectrometer using an electron multiplier collector. Blanks were analysed at the start and in between every run. Mass discrimination during the sample run was monitored and calibrated by analysis of air standards. Mass discrimination, nucleogenic interference and atmospheric contamination were corrected using MassSpec software (version 8.058). Ages were calculated using the decay constant factors after Renne et al. (2011) and yields an age of 107.7 ± 8.8 ka (MER149A) and 87 ± 16 ka (MER147-2D) with 2σ uncertainty.

One sample of charcoal embedded within a BBTM tephra deposit was sampled for accelerator mass spectrometry radiocarbon dating. The conventional age of 871 ± 24 ^{14}C yr BP was calibrated using Oxcal 4.4 (Bronk Ramsey 2009) using the IntCal20 calibration curve (Reimer et al. 2020). The calibrated radiocarbon age gives an age of 1190 ± 36 cal yrs BP (760 ± 36 CE) with a 95.4% probability interval.

After constraining the tephrostratigraphy, the tephra fall volume of individual deposits was estimated for some major eruptions by manually constructing isopachs, based on 4 to 10 data points. We calculated the minimum bulk deposit volumes using the Pyle (1989) and Legros (2000) method.

4. Results

4.1. Field stratigraphy and Geochronology

We identify 27 individual volcanic deposits that are all interpreted to be the products of separate explosive eruptions. The deposits are distinguished based on lithological (e.g. componentry, clast textures, glass geochemistry) and depositional characteristics. Most units are correlated at a local/sub-regional scale based on field and laboratory data, except for some of them (at least seven; section 4.1.8). In the following descriptions, the deposits are categorized on their interpreted source vent/area and described from the oldest to youngest for each category. Based on the distance from the vent area, the outcrops are defined as very proximal (<5 km from the vent), proximal (5-10 km), medial (10-30 km) and distal (>30 km). The identified stratigraphic units are labelled in systematic stratigraphic order from base to top, starting with two letters that represent the source vent (e.g. the basal pumice unit from Baricha is Ba-P1 and is overlain by Ba-P2). The location of each section is presented on Figure 2 and in supplementary material (SM-3). The overview of the stratigraphic record and unit correlations is shown on Figure 3. Key images and description of representative outcrops (Fig. 4; SM-3), componentry, and petrography (Fig. 5; SM-4) are also displayed on separate figures and all the data is included in the supplementary material. Table 2 represents the main characteristics of all BBTM deposits; descriptions of widely dispersed eruptive units (i.e. major deposits, correlated across at least 5 sections) are given below. In these descriptions, we simply mention the chemical composition of the units to support the correlations, but more details of the geochemistry are given in Section 4.2.

4.1.1. Suke Deposit

The Suke deposit is the oldest pyroclastic BBTM unit identified in the region. The base of the deposit is not observed, but the unit is overlain by a succession of Meki pumice (section

4.1.2) and porphyritic basaltic lava in different sites. Glass compositions of the Suke unit are pantelleritic. The deposit is exposed at only a few locations (MER253 and MER367) in the area of Suke, along a deep gully in the north-central part of the complex (Fig. 2). It has a maximum thickness of 6 m at Suke (MER253) and is very poorly sorted, clast-supported, and fine depleted, with bombs and lithic blocks up to 1 m in diameter of aphyric obsidian, dense pumice and altered lava (Fig. 3a; Fig. 4). About 3 km east of the type locality, in section MER367, the fine-grained component (<2 mm) with both pumiceous and lithic material becomes dominant (>50%). The pumice is light to dark grey and very crystal poor with only <1% of aenigmatite and no other visible crystals. The depositional characteristics indicate that the Suke deposit is an ignimbrite with a lithic lag breccia facies in proximal section MER253, and representative of pyroclastic density currents (PDCs) formed during a caldera-forming eruption. The absence of any datable material (e.g. sanidine phenocrysts) prevents us from constraining the absolute age of the Suke ignimbrite.

4.1.2. Meki Deposit (107.7 ± 8.8 ka)

The Meki deposit is exposed in four places around the town of Meki (Fig. 2). It is also underlain by the Suke deposit and overlain by tephra deposits sourced from Baricha (cf. Section 5.1.3) in the Suke locality (MER253; Fig. 3a). At this latter location, the Meki deposit is separated from both under- and overlaying units by weakly developed palaeosols. The largest outcrop exposes >20 m of pyroclastic deposits in a quarry site near the Ziway-Meki road (MER149 and MER326). There, the basal portion (up to 3 m exposed) of the sequence is a well-sorted, massive, fine to coarse pumice lapilli breccia that is free of accidental lithics. In this lower part of the quarry, at ca. 1660 m asl, distinct sub-horizontal brown staining on the pumice surface is observed over a thickness of ca. 1 m in the MER149 and MER326 outcrops. The middle portion of the deposit is characterised by alternations of well-sorted and poorly sorted fine lapilli breccia units that range between 10 and 90 cm in thickness. The poorly sorted part of the deposit does not maintain a consistent local thickness and becomes very thick (~13 m) in a section west of Meki town (MER327; Fig. 2a). At this section the deposit is poorly sorted, displaying a variety of lenticular and wavy bedding, horizontal laminations (alternation of mm-scale fine ash and lapilli layers), and in places mm-scale sub-parallel to low-angle cross-bedding, with sub-rounded pumice lapilli in a fine ash matrix. The upper ~8 m of the Meki deposit is, again, a massive, well-sorted and lithic-free pumice lapilli breccia with ca. 10% of expanded pumice clasts. The deposit from the Meki section (i.e. MER149) is virtually free of lithics and contains 80-95% pumice clasts (45-90% microvesicular-light grey and ≤40% expanded-dark grey coloured pumice) and 5-20% free crystals (alkali feldspar and aenigmatite) in the finer fractions below 1 mm. The pumice clasts are highly vesicular (ca. 70-75% vesicularity), almost aphyric with ca. 1% phenocrysts of alkali feldspar and aenigmatite, within a microlite-free groundmass. The Meki deposit has distinct pantellerite glass compositions (section 4.2) relative to the Suke deposit, allowing the correlation between the two main sequences in the area of Meki (west of the BBTM complex) and Suke (central part; Fig. 2). At the Suke section, the Meki deposit is represented by three stratigraphic horizons that show coarse lapilli at the base and matrix-dominated massive beds at the top. The lack of an erosive surface or palaeosol between these horizons suggests there was not a significant time gap between their depositions. Both in Suke and Meki, we interpret the lower and upper portions of the deposit as a tephra fall, and the middle part as a diluted PDC that is also interbedded with minor tephra falls. Sanidine crystals from the lower part of the deposit were dated by $^{40}Ar/^{39}Ar$ to 107.7 ± 8.8 ka (Table 1).

4.1.3. Baricha Sequence

The Baricha pyroclastic deposits are relatively widely dispersed to the West and well preserved in different stratigraphic sections. Some major units (i.e. well dispersed; Ba-P3 to Ba-P7) are observed in up to 25 different outcrops that extend 20 km from the summit of Baricha. The Baricha tephra sequence is stratigraphically younger than the Meki deposit, and the deposits commonly have lithics and a small proportion of expanded pumice lapilli. A deep gully (MER147) near Baricha exposes >9 distinct pantelleritic stratigraphic units (Fig. 3a). These units are separated by well-developed, 5 to >20 cm thick palaeosols. Other sections (e.g. MER205, MER301-3 and MER324) expose 6-8 individual deposits that can be correlated with the Baricha type section (MER147). Altogether, there are 5 major and 4 minor eruption deposits attributed to Baricha and sorted from oldest (Ba-P1) to youngest (Ba-P9) in Table 2. The major units are described in further detail here.

Ba-P3 is the oldest major Baricha deposit identified in a few proximal sections. A maximum thickness of ca. 3 m is observed in a section (MER205) located 4.5 km west from the summit. The basal 5-10 cm of the unit is composed of poorly sorted, well-indurated fine ash and accretionary lapilli. Above the bottom ash horizon, the deposit appears as a light grey coloured pumice lapilli breccia, that is well sorted and with massive to cm-scale crude bedding. The upper portion contains occasional pumice bombs (~15 cm) embedded in a sandy to silty cream-coloured horizon that is much more matrix-rich than the lower half of the deposit. The componentry of the middle portion of Ba-P3 shows 80-90% pumice clasts (microvesicular), ≤20% free crystals in the finer fractions (feldspar, aenigmatite and orthopyroxene) below 1 mm and <1% lithics (crystal-rich obsidian). The pumice clasts are highly vesicular (ca. 65% vesicularity), moderately phyric with ca. 6% phenocrysts of alkali feldspar, aenigmatite and orthopyroxene in a glassy groundmass. We interpret the ash unit with accretionary lapilli and middle section of Ba-P3 formed by tephra fall and the upper portion, more matrix-rich, as the result of pedogenesis.

Above Ba-P3, a tripartite Baricha unit (Ba-P4) is exposed in different outcrops with a maximum total thickness of 3 m. The lower meter of the deposit comprises cm-scale alternations of fine lapilli and a yellowish ash bed. The rest of the deposit is massive and contains occasional pumice bombs of ~20 cm diameter in very proximal outcrops. The massive portion of the unit overlies a subtly normally graded 30 cm thick subunit; and it is composed of a clast-supported, poorly sorted, very coarse lapilli breccia. The componentry of the massive portion shows 45-80% pumice clasts (45-75% microvesicular, <5% expanded and ≤1% tube pumice), 10-35% free crystals (feldspar, aenigmatite, amphibole and Fe-Ti oxides) in the finer fractions and ≤10% lithics (crystal-rich obsidian, altered lava and ignimbrite). The pumice clasts are moderately vesicular (65% vesicularity), and almost aphyric, with <1% phenocrysts of alkali feldspar and aenigmatite, in a microlite-poor groundmass. The depositional characteristics indicate that the Ba-P4 deposit is a fallout tephra.

Ba-P5 is a widespread deposit identified to the West of Baricha. It is preserved in both proximal and medial outcrops, with a maximum thickness of 2.7 m. The unit is typically lithic-rich at the base and shows a gradual decrease in lithic proportion and other facies variations upwards in the stratigraphy. The bottom and top-third portions of the unit are massive while the middle part shows cm-to-dm-scale diffuse bedding of generally well sorted pumice lapilli breccia. In medial outcrops (e.g., MER229 and MER325), the deposit shows two subunits with poorly developed normal grading. The componentry shows that Ba-P5 contains 55-75% pumice clasts (55-75% microvesicular, ≤20% expanded and ≤1% tube pumice), 5-40% free crystals (feldspar, aenigmatite, pyroxene, amphibole and Fe-Ti oxides) in the finer fractions and ≤5% lithics (crystal-rich obsidian, altered lava and ignimbrite). The pumice clasts are moderately vesicular (50-65% vesicularity) with <10% phenocrysts of alkali feldspar, aenigmatite, orthopyroxene and amphibole, and a glassy groundmass. The Ba-P5 tephra deposit is interpreted as a fallout tephra unit. A bulk sample of this unit was collected at section MER147 for single-crystal (alkali feldspar) $^{40}Ar/^{39}Ar$ dating, and yields an age of 87 ± 16 (2σ) ka (Table 1).

Ba-P6 is a well-preserved Baricha deposit overlying Ba-P5 and separated from it by a palaeosol. A maximum thickness of ~4 m is measured in a proximal gully section (MER302). In most outcrops (e.g. MER205 and MER302), Ba-P6 shows dm-scaled multiple horizons of well-sorted coarse to fine pumice lapilli with abrupt grain size transitions. The componentry shows that Ba-P6 is almost lithic-free (≤2% of crystal rich obsidian, altered lava and ignimbrite) and contains 50-70% pumice clasts (50-70% microvesicular and <10% expanded pumice) and ca. 30% free crystals (feldspar, aenigmatite, amphibole and Fe-Ti oxides) in the finer fractions below 1 mm. The pumice clasts are moderately vesicular (50% vesicularity), with <10% phenocrysts of alkali feldspar, aenigmatite and amphibole, set in a glassy groundmass. The depositional characteristics indicate that the Ba-P6 deposit is a tephra fall deposit.

Ba-P7 is a light grey pumice deposit confirmed in 15 different stratigraphic sections. The unit is 5 m thick at 4 km distance from the summit (MER205). The bottom of Ba-P7 is a matrix-supported and cream-coloured pyroclastic deposit in medial outcrops (at ~15 km distance from the source) and a fallout unit in proximal outcrops. The main part of the Ba-P7 unit is diffusely dm-scale bedded, but overall normally graded and poorly sorted pumice lapilli breccia. In the upper half of the unit, pumice bombs up to 10-15 cm diameter are present. The componentry shows that Ba-P7 is almost lithic-free (≤2% of crystal rich obsidian, altered lava and ignimbrite) and contains 65-90% pumice clasts (65-85% microvesicular, ≤2% expanded and ≤2% tube pumice) and 5-30% free crystals (feldspar, aenigmatite and Fe-Ti oxides) in the finer fractions. The pumice clasts are moderately to highly vesicular (50-55% vesicularity), and almost aphyric with <1% phenocrysts of alkali feldspar and aenigmatite in a glassy groundmass. We interpret Ba-P7 as a PDC deposit (in medial outcrops) overlain by a tephra fall.

The youngest Baricha deposit found, Ba-P9, is a minor unit underlain by a cream-coloured, matrix-supported and undulatory bedded horizon that is interpreted as a PDC deposit. In outcrop MER308 a piece of black, friable charcoal was recovered from the upper part of this PDC deposit. A radiocarbon date of the charcoal yields an age of 1190 ± 36 cal yr BP (760 ± 36 CE).

In summary, at Baricha, we identify in total seven pumice fall deposits (Ba-P1, Ba-P3 to Ba-P8) and another two composite deposits that have both tephra fall and PDC units (Ba-P2 and Ba-P9; Table 2).

4.1.4. Oda Sequence

A sequence of pyroclastic deposits is exposed in the vicinity of the Oda crater and attributed to this centre. Oda has a well-developed 0.9 x 0.78 km crater partially filled by a small lake (Fig. 2a). The stratigraphic section to the SE of the summit crater (MER336) displays 8 different units with pantellerite-comendite glass compositions (Fig. 3). The tephra deposits are generally poorly preserved in medial and distal sites (>10 km). Two major (Od-P4 and Od-P5) and five minor units are assigned to Oda, each of them separated by poorly to well-developed palaeosols (Table 2).

Od-P4 is a pumice lapilli breccia deposit with cm-scale bedding and normal grading within each bed set in the bottom portion before becoming massive in the top ~30 cm. A maximum thickness of 3 m is observed in MER336. In several sections (e.g. MER231), the bottom 10-30 cm is marked by a lithic-rich poorly sorted ash-dominated horizon (i.e. tuff). The componentry shows that Od-P4 contains 60-80% pumice clasts (60-80% microvesicular and ≤1% tube pumice), ≤25% lithics (hydrothermally altered lava, glassy obsidian and ignimbrite) and 10-20% free crystals (feldspar, aenigmatite and Fe-Ti oxides) in the fractions below 1 mm. The pumice clasts are moderately to highly vesicular (55-65% vesicularity), and sparsely aphyric with ≤3% phenocrysts of alkali feldspar, clinopyroxene, amphibole and aenigmatite in a glassy to microlite-poor groundmass. The mineralogy of the microlites is similar to that of the phenocrysts. Od-P4 is interpreted as a PDC deposit overlain by a tephra fall.

Above Od-P4, a relatively well-preserved deposit (Od-P5) is exposed. Od-P5 is 3.5 m thick at Oda's flank and still ≥40 cm at 6 km distance (MER237) from the volcanic centre. The unit is characterised by a massive, fine pumice lapilli breccia, that is poorly sorted, lithic-rich and comprises few distinctly larger pumice clasts (~3.5 cm). The componentry shows that Od-P5 is lithic-poor (≤3% of hydrothermally altered lava and glassy obsidian) and contains 60-70%

pumice clasts (60-70% microvesicular and ≤1% tube pumice) and 5-35% free crystals (feldspar, quartz, aenigmatite, pyroxene, amphibole and Fe-Ti oxides) in the finer fractions. The depositional characteristics indicate that Od-P5 is a tephra fall deposit.

4.1.5. Bora Sequence

Bora deposits are generally poorly preserved and found in the south western part of the BBTM complex. A deep gully (MER231) located at 11 km southwest of the Bora edifice exposes two major and one minor deposit with pantelleritic-comenditic compositions (Table 2, Fig. 4d). The pyroclastic deposits can be correlated with outcrops that extend to at least 14 km distance from the summit. The Bora sequence lies entirely on top of the Oda sequence and can be distinguished from the latter by its lithic-poor nature and rare hydrothermally altered lithics.

Bo-P2 is exposed in only a few proximal outcrops. The unit is a cm-scale bedded, well-sorted pumice lapilli breccia, and contains occasional pumice bombs (~15 cm in diameter). The deposit appears light grey at the base, and gradually progresses to a cream-coloured, lenticular-bedded, poorly sorted unit with sub-rounded pyroclasts towards the top. A maximum thickness of 2.5 m is observed in outcrop (MER231) located 11 km from the vent. The componentry of Bo-P2 shows 60% pumice (60% microvesicular and 1% tube pumice), ≤15% free crystals (feldspar, quartz and Fe-Ti oxides) in the finer fractions and <8% lithics (hydrothermally altered lava, glassy obsidian and ignimbrite). The pumice clasts are entirely aphyric and moderately vesicular (ca. 60% vesicularity). We interpret the lower half portion of Bo-P2 to be formed by tephra fall and the upper portion to result from the main unit’s weathering.

Bo-P3 is a relatively widespread Bora deposit. The unit is an entirely massive, poorly sorted coarse pumice lapilli breccia. The maximum thickness of the deposit is 3 m and thins out to a minimum of 65-70 cm in medial outcrops at 13 km distance from the summit. The componentry of Bo-P3 shows it to be almost lithic-free (≤1% altered lava and glassy obsidian), and contain 90% pumice (80% microvesicular, 5% expanded and 3% tube pumice) and 5% free crystals (feldspar, aenigmatite, pyroxene and Fe-Ti oxides) mainly concentrated in the finer fractions. The pumice clasts are almost aphyric (<0.5% alkali feldspar, aenigmatite and orthopyroxene), moderately to highly vesicular (45-75% vesicularity), and have a glassy groundmass. The depositional characteristics suggest that Bo-P3 is a pyroclastic fall deposit.

4.1.6. Werdi Sequence

Werdi deposits are exposed in a few outcrops located in the central and northern parts of the volcanic complex. A gully section (MER309; Fig. 4e) located in the vicinity of the southern Lake Koka shore provides an apparently near complete overview of the Werdi sequence. At MER309 three Werdi units, 2 major (Wd-P1 and Wd-P2) and 1 minor (Wd-P3; Table 2), are observed. The Werdi sequence overlies the Suke deposits and is separated from it by well-developed palaeosols. The Werdi deposits are easily identified by the bluish-grey colour of the pumice clasts and pantelleritic-comenditic compositions.

Wd-P1 sits stratigraphically above the Suke deposit (MER309) and an obsidian lava flow (MER246). The unit is bedded at the cm-scale, poorly sorted, lithic-poor and composed of coarse ash to pumice lapilli. Wd-P1 has a maximum thickness of 15 m and contains occasional pumice bombs (~10 cm) in very proximal outcrops. Wd-P1 contains ca. 83%

bluish-grey pumice (microvesicular), ca. 10% lithics (hydrothermally altered lava and crystal-rich obsidian), and ca. 5% free crystals (feldspar, aenigmatite, pyroxene and amphibole) in the grain size fractions below 4 mm. Wd-P1 likely originates from a tephra fall.

Wd-P1 is overlain by another 35 cm thick Werdi unit (i.e. Wd-P2) in the MER309 outcrop. In outcrop MER246, Wd-P2 is underlain by crystal-rich obsidian lava. The unit appears as a lithic-poor, well-sorted and massive coarse pumice lapilli breccia. In section MER245 the top part of this unit shows normal grading. The componentry of Wd-P2 shows it to be almost lithic-free (<5% altered lava, glassy obsidian and ignimbrite), with ca. 70% bluish-grey pumice (microvesicular) and ca. 20% free crystals (feldspar, aenigmatite and Fe-Ti oxides) in the finer fractions. The pumice clasts are almost aphyric (ca. 1% alkali feldspar and aenigmatite), moderately vesicular (50% vesicularity), and have a glassy groundmass. The depositional characteristics indicate that Wd-P2 represents a pyroclastic fall.

4.1.7. Tullu Moye Sequence

Tullu Moye deposits are exposed in the heavily faulted eastern zone of the volcanic complex. Two different Tullu Moye units are identified above well-developed palaeosols in most outcrops. Both units are characterised by their distinct white pumice clasts of comenditic composition. TM-P2 is the youngest and main Tullu Moye deposit that overlies TM-P1 (Table 2). The two units are separated by a palaeosol (MER152), but in some proximal outcrops an 80 cm thick scoria lapilli (interpreted as a fall) deposit is interbedded between the two pumice horizons. TM-P2 is widespread to the West and has a maximum thickness of 2 m in proximal outcrops (e.g. MER240). TM-P2 is a massive, poorly sorted pumice lapilli breccia, and contains occasional pumice bombs (up to 15 cm). The deposit is almost lithic-free (<3% hydrothermally altered lava and glassy obsidian), and contains ca. 70-100% white pumice (70-100% microvesicular, ≤1% expanded and ≤1% tube pumice) and ≤20% free crystals (feldspar, pyroxene, amphibole and Fe-Ti oxides) in the finer fractions. The pumice clasts are almost aphyric (ca. 2% alkali feldspar, clinopyroxene and amphibole), moderately vesicular (60% vesicularity), and have a glassy groundmass.

4.1.8. Additional deposits

Besides the well-dispersed BBTM tephra deposits described in sections 4.1.1 to 4.1.7, a significant number of deposits are found in single outcrops without having a correlative in other sites. Most of these deposits are exposed on the flanks of monogenetic pumice cones. At least 11 separate vent / cones are identified around the larger edifices such as Bora, Baricha and Tullu Moye (Fig. 2a). These are interpreted as pumice cones which are also common at Aluto volcano (e.g. Clarke et al. 2020). The maximum thickness of the deposits ranges from <1 m to 8 m. These deposits are characterised by massive, poorly sorted pumice lapilli breccia with occasional pumice bombs (up to 8 cm in diameter) and expanded pumice clasts. The deposits identified at outcrops MER209 and MER150 shows an alternation of tephra layers with relative variations of sorting and stratification. The lab-based componentry analysis shows that these deposits contain 70-95% pumice clasts (60-90% microvesicular, ≤10% expanded and <10% tube pumice), <25% lithics (altered lava, glassy obsidian and ignimbrite) and <20% free crystals (feldspar, quartz, aenigmatite and Fe-Ti oxides) in the finer fractions. The pumice clasts are rhyolitic in composition, moderately vesicular (ca. 35-60% vesicularity) and almost aphyric (<3%).

In addition to these units attributed to pumice cones, there are some other deposits observed in the BBTM volcanic complex that also have no correlatives. At least seven tephra deposits are identified in the regions around Baricha, Oda and Tullu Moye. At MER201, near the Baricha edifice, two massive pumice lapilli breccia layers have thicknesses of 1.3 m and ~2 m, but have not been identified elsewhere. At section MER 237, three relatively thin (max. 40 cm), massive, lithic-poor fine lapilli breccia units alternate with a reworked pyroclastic deposit. In the eastern rift escarpment, at MER 385, ~6 km E of Tullu Moye, two tephra layers with pantellerite-comedite compositions are found. The field data and componentry of these deposits are distinct from those of any BBTM major units.

4.2. Glass chemistry

4.2.1. Major element composition

Major element glass compositions of selected proximal, medial and distal tephra (pumice) deposits from the BBTM region reveal that the parental melts consistently have alkali-rich rhyolite compositions (Fig. 6a). The average major element compositions of the selected tephra deposits are presented in Table 3, with the full dataset in Supplementary information (SM-2). All compositions are peralkaline and are classified as either pantellerite or comendite (Fig. 6b). The latter composition is characteristic of Tullu Moye tephra only, whereas all deposits from Baricha, Suke and Meki are entirely pantelleritic. The glass compositions of Oda, Werdi and Bora tephra deposits, straddle the comendite-pantellerite boundary (Fig. 6b). Except for the distinct comenditic Tullu Moye glasses, all BBTM glass major element compositions overlap with those of Aluto, Corbetti and Gedemsa tephra deposits (Fig. 6, 7; Martin-Jones et al. 2017; Fontijn et al. 2018; McNamara et al. 2018).

Each pantelleritic deposit has a tight homogeneous composition within the larger pantellerite cluster (70.1-77.9 wt% SiO_2, 6.0-14.8 wt% TA; 7.6-11.7 wt% Al_2O_3, 4.3-7.3 wt% FeO). However, different deposits may overlap in composition, complicating correlations based on major element glass composition alone. In general, Baricha deposits tend to have the highest Total Alkali and FeO contents and are also distinct in other major element contents, e.g., TiO_2 (Fig. 7b). Meki and Suke tephra predominantly have glass compositions with a higher TiO_2 (>0.23 wt%) and CaO (>0.2 wt%) content relative to those of Baricha. Meki and Suke are also distinguished from each other, especially by their Al_2O_3 and FeO contents (Fig. 6b, 7a-d). There are no discernible chemical differences between the individual Baricha tephra units.

The Tullu Moye pyroclastic deposits are mainly composed of comenditic glass. This tephra group is slightly less evolved (lower SiO_2) compared to the other BBTM tephra deposits. It is characterized by a lower amount of SiO_2 (71.3-73.6 wt%), FeO (1.6-3.5 wt%) and a distinctly higher amount of Al_2O_3 (12.4-15.1 wt%; Fig. 6). These two Tullu Moye deposits (TM-P1 and TM-P2) each also have highly distinct glass compositions, as revealed by their separate clusters in all major element bivariate diagrams (Fig. 6-7). TM-P1 is characterised by a higher TiO2, Al_2O_3, CaO, K_2O (Fig. 7) and MgO (not plotted) contents relative to TM-P2. TM-P2 is relatively more evolved than TM-P1 and contains higher contents of SiO_2, Na_2O and FeO (Fig. 6-7).

The tephra deposits from Oda, Werdi and Bora show significant compositional heterogeneity in the glass major element composition. The melt compositions span from comenditic to pantelleritic and many fall near the compositional divide on the peralkaline classification diagram (Fig. 6b). Many samples in this population overlap with the highly evolved (high-SiO_2) end of the pantelleritic rhyolites. The FeO and Al_2O_3 contents can be used to discriminate some of the tephra units in this population. For example, glasses from Od-P1, Od-P2, Od-P3, Od-P4 and Wd-P2 have slightly lower FeO (<5 wt%) and higher Al_2O_3 (>9.1 wt%) contents than the other samples in this group. In contrast, deposits such as Od-P7, Wd-P3 and Wd-P1 have higher FeO (>~6 wt%) and lower Al_2O_3 (<9 wt%) contents. The other tephra units in this population show a wide variation of FeO (3.9-7 wt%) and Al_2O_3 (7.8-11 wt%) contents. The other major element contents like silica and the total alkali contents show less variation (Fig. 6a). One uncorrelated tephra unit exposed at MER150 shows a similar (comenditic) composition to Oda and Werdi deposits (Fig. 6-7). The field, componentry and petrographic data show that this MER150 tephra is likely sourced from a small pumice cone located in the SW part of the complex. In this deposit, there is a strikingly clear chemical variation from comendite to less evolved pantellerites through the stratigraphy.

4.2.2. Trace element composition

To investigate the compositional variability of the BBTM tephra deposits in more detail, trace element glass data were obtained on a selection of samples already analysed by EPMA. The average glass trace element compositions of the analysed tephra layers are presented in Table 3, with the full dataset in Supplementary information (SM-5). The geochemical group revealed by the major element data (section 4.2.1) are also evident in the trace element compositions (Fig. 8). The pantelleritic samples (e.g. Baricha) have systematically higher concentrations of incompatible trace elements (e.g. Zr, Rb, Y, La, Ce) than the comendites (e.g. Tullu Moye). The trace element glass data further highlight significant compositional variation within the pantellerite population between Baricha and the other tephra deposits (Fig. 8). Baricha glasses have higher Zr (>1500 ppm), Rb (>200 ppm), Y (>150 ppm), La (>150 ppm) and Ce (>300 ppm) contents relative to those from Oda, Suke, Meki and Bora. Other trace elements such as Nb, Cs, Pb and other REEs are also more enriched in the Baricha samples. The only analysed trace elements that are depleted in the pantellerites relative to the comendites are Ba and Sr. The Ba and Sr contents indicate, again, that the oldest Tullu Moye unit (TM-P1; Ba: 550 ± 50 ppm and Sr: 50 ± 10 ppm) is compositionally distinct from the youngest unit (TM-P2; Ba: 400 ± 50 ppm and Sr: 10 ± 3 ppm) (Fig. 8).

Unlike the major element compositions, Aluto tephra trace element compositions (McNamara et al. 2018) show distinct differences with those of Baricha, Meki and Suke samples, especially in Ba and REE content (Fig. 8).

4.3. Eruptive Volume and Magnitude

The tephra fall volume for 12 major eruptions is estimated by manually constructing isopach maps (Fig. 9). Unfortunately, the Suke, Meki and 13 post-caldera deposits are not sufficiently exposed over multiple locations to provide an estimate on volume. Two deposits (Ba-P4 and Ba-P5) were identified in multiple locations covering a large enough area so that more than two isopach contour lines could be constructed (Fig. 9a-b). We calculated the minimum bulk deposit volume for these two deposits using the 1-segment exponential thickness decay model of Pyle (1989). The limited exposure does not allow multiple segments to be identified on a thickness-area trend (Bonadonna et al. 1998) and thus other methods to estimate deposit volume, typically requiring additional constraints (e.g.

Bonadonna & Houghton 2005), are not suitable in this case. For the 10 remaining deposits identified in multiple locations (Ba-P2, Ba-P3, Ba-P6, Ba-P7, Od-P4, Od-P5, Wd-P2, Wd-P1 and TM-P2), only one or two contour lines can be inferred, and for these we use the Legros (2000) one-isopach method to estimate their minimum bulk volume. The bulk volume estimation of these deposits falls in the range 0.007 km^3 to 1.1 km^3. The componentry data of these deposits indicates the lithic content is very low (<10% in the fraction below 4 mm) compared to the juvenile proportion. Therefore, we only considered the pumice when converting the bulk deposit volume to a dense rock equivalent (DRE) volume, by assuming 2300 kg/m^3 rhyolite melt density (Fierstein & Hildreth 1992) and 470 kg/m^3 average bulk density as measured on BBTM deposits. The DRE volume of major BBTM eruptions is thus estimated between 0.001 km^3 to 0.22 km^3. These estimates were then used to calculate minimum magnitude of these eruptions using the following relationship: Magnitude = $\log_{10}$ [erupted mass, kg] - 7 (Pyle 2015). Based on the preserved deposits, most magnitude estimates range from 3.9 to 4.7 for eruptions from Werdi, Oda, Bora and Baricha (see supplementary material SM-6). The youngest Tullu Moye eruption however has a lower minimum magnitude of 2.5. The three Baricha eruptions that are most widespread, up to 20 km west of the edifice (Ba-P4, Ba-P5 and Ba-P7) have a minimum estimated magnitude of 4.6 to 4.7.

5. Discussion

5.1. Tephrostratigraphy and Correlation

Eruptive deposits from the BBTM volcanic complex overlay a series of older volcanic rocks (Fig. 2b). The base of the BBTM sequence observed in the field (this work) and in shallow wells (Ayele et al. 2002) comprises welded ignimbrite and lavas of different composition (rhyolite, trachyte and basalt). This series blankets the rift floor and in different parts of the MER is known as the Nazret unit (Kazmin & Berhe 1978). An obsidian flow and ignimbrite of this series collected near Tullu Moye volcano yields a late Pleistocene age of 1.58 ± 0.2 Ma (WoldeGabriel et al. 1990) which is coeval to the development of the Wonji Fault Belt (WFB) along the MER axis (1.6 Ma; Ebinger & Casey 2001). This older unit is related to pre-BBTM volcanism and may be associated with the start of tectono-magmatic focusing along the axial zone of the MER.

The oldest deposit recognised in our work, the Suke deposit, is primarily composed of large boulders and blocks of poorly-vesiculated pumice and obsidian lithics at the type section (MER253; Fig. 2). A few kilometres SE from the type section, this unit becomes finer-grained with a more prominent ashy matrix. We interpret the Suke deposit as an unwelded ignimbrite unit, with its very coarse facies a “pumice and lithic lag breccia”, commonly interpreted to represent the onset of caldera collapse (e.g. Druitt & Sparks 1982; Jordan et al. 2018; Seggiaro et al. 2019). The dense and coarse blocks, possibly partially related to vent erosion or widening, thus segregated from the PDCs which then carried relatively finer material further from the source (Druitt & Sparks 1982; Druitt 1985; Walker 1985). The juvenile volcanic products have no datable material (i.e. sanidine) and thus the absolute age of the Suke caldera-forming event remains unconstrained.

The Meki deposit directly overlays deposits of the Suke caldera-forming eruption. A faint weathered horizon at the top of the Suke deposits indicates a hiatus and testifies that the two units represent different eruptions. The glass compositions further support this interpretation, with a clear difference in Al_2O_3 and FeO contents between the two deposits

(Fig. 6b, 7a-d). The Meki deposit is a very thick fall (>20 m; cumulative of at least two horizons) and PDC (>13 m) deposit at 20-25 km distance from the centre of BBTM volcanic complex. At these medial locations (20-25 km from the vent) three main distinct horizons are observed in the Meki deposit. These horizons are massive tephra fall at the base and top, separated by alternating tephra fall and poorly sorted PDC deposits. Across this sequence, the deposits are characteristically lithic-free, which can be partially used as a diagnostic feature to identify them in the field. The brown surficial staining on the pumice deposits at ca. 1660 m asl. and the deposits age (107.7 ± 8.8 ka) suggest that the Meki eruption possibly pre-dates with the lake-level high stand of the oldest megalake phase that covered most of the Central MER (Benvenuti et al. 2002), including the western portion of the BBTM volcanic system.

Despite the lithic-free nature of the deposits, and relative limited exposure preventing volume estimates, the large thickness of the deposits and distance to the source, leads us to suggest that the Meki eruption may have led to another caldera collapse. Other volcanic complexes in the Central MER had caldera-forming eruptions at 180 ± 30 ka (Corbetti), 306 ± 12 to 316 ± 19 ka (Aluto) and 282 ± 110 ka (Gedemsa; Hutchison et al. 2016a, b). The 107.7 ± 8.8 ka Meki eruption may thus be the youngest caldera-forming event in the central sector of the MER, and is also notably younger than the hypothesised ignimbrite flare-up window (320 to 170 ka) proposed by Hutchison et al. (2016b). Additional age constraints on Central MER caldera-forming eruptions, such as the Suke ignimbrite, are required to test the flare-up hypothesis. Due to extensive post-caldera activity, the dimensions and geometry of the inferred caldera associated with the large Suke and Meki eruptions are difficult to trace. However, there are some possible remnants visible on the hill-shade map on Figure 2a and noted by Korme et al. (2004) as "Tullu caldera" that requires further study to establish any association with the large eruptions documented here.

As reported in several case studies, caldera-forming eruptions may experience a transition from a single-vent phase to a subsidence-related multiple vent phase along a ring structure in the post-caldera sequence of events (e.g. Druitt & Sparks 1984; Lipman 1984; Heiken & McCoy 1984; Hildreth & Mahood 1986). The BBTM experienced both effusive and explosive volcanism during its post-caldera stage, forming both lavas and pyroclastic deposits (Di Paola 1972; Fontijn et al. 2018; this work). The widespread tephra deposits were identified to originate from the Baricha, Bora, Oda, Werdi and Tullu Moye edifices (section 4.1). In proximal sequences, we find deposit characteristics, such as the presence of ballistics, expanded clasts, coarse-grained pumice and lithic breccias. The stratigraphic relationship between the caldera-forming and post-caldera deposits can be observed in some sections, with palaeosols developed on top of the former, indicating a hiatus. One post-caldera eruption in the Baricha sequence (Ba-P5) was dated at 87 ± 16 ka and is underlain by at least 4 more post-caldera eruptions. The pause in volcanic activity following the youngest caldera-forming eruption (Meki) is thus at most on the order of thousands to a few tens of thousands of years at BBTM. This is distinctly shorter than the inferred 250 ky hiatus identified by Hutchison et al. (2016a) at Aluto following the caldera-forming event.

The Meki deposit is entirely lithic-free, whereas the post-caldera deposits contain some lithics. This may be related to a restructuring of the plumbing system caused by the caldera collapse (e.g. Hildreth & Mahood 1986), competence variation of rocks at fragmentation depth (Aravena 2017) and/or possible presence of a lithic-dominated deposit horizon other than the Meki one at depth. The lithic components in the post-caldera deposits are mainly composed of green ignimbrite, rhyolite, basalt and obsidian lava. The subsurface geology of BBTM, observed in the shallow drill cuttings (Ayele et al. 2002; Fig. 2b) shows an ignimbrite and lava series similar to these lithic components. This may indicate that the lithic components in the deposits are mainly sourced from vent erosion at a relatively deep level (5-170 m).

The glass composition of Suke, Meki, Baricha and some Bora tephras are pantelleritic and show a lot of similarities (e.g. 70-78 wt% SiO_2), even in the trace element contents. This creates a practical complication for the correlation of the deposits based on glass chemistry alone. This chemical homogeneity is commonly found in highly evolved tephra deposits (e.g. Toba: Smith et al. 2011; Ciomadul: Harangi et al. 2020; Aeolian Islands: Albert et al. 2017; Corbetti: Fontijn et al. 2018; Martin-Jones et al. 2017). Other characteristics, e.g. componentry, are thus required to help correlate the units. Notably, the Baricha tephra deposits are the only units that do not contain any lithics of hydrothermally altered reddish lava, in stark contrast to the Bora units. In addition, the absence of lithics in Meki is diagnostic and allows it to be distinguished from other BBTM deposits.

The pumice cone deposits that outcrop around the major centres likely represent relatively small-scale eruptions. They are characterised by significant deposit thinning over short spatial distance and fall-PDC successions consistent with alternating sustained columns and plume collapses (Clarke et al. 2019).

The glass major element chemistry of the BBTM deposits overlaps with that of the Aluto and Corbetti deposits. However, the trace element data, especially Ba and some REEs, differ and can be used to discriminate BBTM from Aluto compositions. The generally higher incompatible trace element concentrations of Meki indicate that the melt was more evolved than at Aluto.

5.2. BBTM Eruptive Frequency

Based on the established tephrostratigraphic framework, we can constrain the overall eruptive frequency of BBTM. BBTM experienced at least two caldera-forming eruptions, the most recent one (Meki) at 107.7 ± 8.8 ka. After this eruption, post-caldera volcanic centres such as Baricha, Bora, Oda, Werdi and Tullu Moye together erupted explosively at least 25 times within the last 100-116 ky and that left pyroclastic deposits that can be traced in multiple locations. In addition, more than 7 non-correlated units are identified, each likely representing a single eruption. Therefore, on average at least one explosive eruption occurred per 3000-4000 years in the BBTM volcanic system. Of these post-caldera explosive eruptions, three are attributed to Bora, eight to Oda, three to Werdi and two to Tullu Moye. Additionally, Baricha volcano was the source of at least nine eruptions. For two Baricha eruptions, we were able to constrain an absolute age: the Ba-P5 eruption occurred at 87 ± 16 ka and the Ba-P9 eruption (the youngest that is preserved in the record) occurred at 1190 ± 36 cal yr BP. This shows that Baricha had at least 5 eruptions within the first ca. 20,000 years after the Meki eruption and then at least 4 more eruptions since ca. 87 ka. Since younger and/or larger eruption products are expected to be preferentially preserved relative to older and/or smaller deposits (Brown et al. 2014), the geological records are may be biased. The chronological (and magnitude) constraints on our present stratigraphic framework are unfortunately too incomplete to allow inferring any changes in eruption frequency or rate through time at BBTM. Our magnitude (Section 4.3) estimations suggest that the BBTM volcanic complex has experienced at least 11 post-caldera explosive eruptions with a magnitude of 4 or above (Section 4.3) within the last ca. 100,000 years. Note that our evaluations of eruption frequency and magnitude do not take into account the effusive eruptive products and are also based on minimum frequency and eruptive volume estimations that are certainly influenced by deposit preservation and/or deposit thinning behaviour (e.g. Bonadonna & Houghton 2005). Regardless, compared to other volcanic complexes in the region, such as Aluto and Corbetti, BBTM seems less frequently active in terms of explosive eruptions. However, BBTM may be more frequently active, and characterised by higher-magnitude post-caldera eruptions, compared to the volcanic systems located further north (e.g. Boset-Bericha and Fentale), which experienced several effusive and a more limited number of explosive eruptions in their recent past (e.g. Fontijn et al. 2018; Siegburg et al. 2018). The combined terrestrial and lacustrine records of Corbetti tephra indicate an explosive eruption every ca. 700-1000 years (Fontijn et al. 2018; Martin-Jones et al. 2017). The lacustrine record provides detailed constraints on the Holocene eruptive history of the volcano by supplementing the terrestrial records (Martin-Jones et al. 2017). The Wendo Koshe Younger Pumice (WKYP) has an estimated minimum volume of 1.3 km^3 (Rapprich et al. 2016; Fontijn et al. 2018), or a magnitude of 4.8 using the same approach as above. In the post-caldera phase, at least during the Holocene, Aluto had an average of 3 eruptions per 1000 years (Martin-Jones et al. 2017; Fontijn et al. 2018; McNamara et al. 2018). Considering the rapid thinning trend of the relatively well-documented Qup deposit, Fontijn et al. (2018) roughly estimated a magnitude of 3 for this pumice cone eruption. There is very little information regarding eruption magnitude for other volcanoes in the MER to make a quantitative comparison. However, from the available information (WKYP: M=4.8 and Qup: M~=3) we conclude that BBTM has eruptions of at least comparable magnitude than Corbetti and Aluto in their post-caldera phase.

5.3. Hazard Implications

The tephrostratigraphic record of BBTM provides evidence for at least two major caldera-forming events and 25 moderate-scale explosive eruptions. The spatial distribution of the deposits of caldera-forming eruptions is poorly constrained because of the abundant post-caldera deposits that conceal them. The second caldera-forming eruption, Meki, has better exposures that document its tephra dispersion. This eruption deposited >20 m tephra fall and >13 m PDCs at medial locations, and >1.1 m tephra fall at distal regions. The established frequency-magnitude information in section 5.1 indicates an explosive eruption occurs from BBTM at least every 3000-4000 yrs. The isopach maps of the well-dispersed post-caldera deposits (Ba-P4 and Ba-P5) indicate dispersion of tephra up to at least 20 km from the volcanic centre, for example in the town of Alem Tena, where deposits are still 1 m thick. These eruptions also accumulated up to 5 m thick deposits in the proximal exposures located within 4 to 5 km of the vent. Oda emplaced clast-supported to matrix-supported PDCs during the penultimate identified eruption (Od-P7). This deposit is identified in a valley that was formed by an intermittent stream that feeds Ziway Lake. Near the base of the Oda edifice, it is 16 m thick and 10 km away it still is 1.5 m thick. In general, from the spatial distribution of the pyroclastic deposits, we can conclude that several BBTM eruptions covered a surface with a radius of at least 25 km.

Within this 25 km radius from any of the main centres, there are numerous urban and rural settlements with highly variable population densities (Fig. 2a). The towns of Alem Tena (10 km from Baricha), Meki (20 km from Bora), Ogolcho (12 km from Oda) and Iteya (11 km from Tullu Moye) are all located within this radius from at least one of the main volcanic vents. Total estimates of around one hundred thousand people are living in these towns and the surrounding rural areas, with many of them highly dependent on agriculture (CSAE 2007). In the towns, with the exception of Iteya, 1 to 20 m thick tephra fall has been deposited during past eruptions. The area is also exposed to tephra fall hazard in the future, and this could cause a major threat to human health and livelihoods, buildings and other infrastructure, economic activities, and ecosystems (e.g. Spence et al. 2005; Wilson et al. 2012). To the West of Meki and Ogolcho, PDC deposits with thicknesses between 1.5 to 13 m also indicate an additional potential volcanic hazard to the BBTM region.

Detailed volcanic hazard assessments can be useful for land-use planning and development of mid-to-long-term risk mitigation strategies. Volcanic hazard maps are often to a large extent based on a volcano's past eruptive history (e.g. Calder et al., 2015). Our current data provide some initial constraints on frequency and magnitude of past eruptions at BBTM, the extent of volcanic deposits inundation and possible related volcanic hazards to the nearby region. Given the high population density and presence of critical infrastructure (e.g. Tullu Moye geothermal facilities) our results may be used as a background for future research in the direction of generating more detailed, potentially probabilistic, volcanic hazard assessment (e.g. Clarke et al. 2020; Tierz et al. 2020) or volcano monitoring activities.

6. Conclusion

A detailed study on the tephrostratigraphic framework of the BBTM tephra deposits has enabled us to reconstruct the past explosive activity of the volcanic complex. Here we present the first detailed stratigraphic record of the explosive eruptions experienced in the BBTM volcanic complex. The field data, glass chemistry (major and trace elements), componentry and petrographic data allow us to identify 27 eruptions that include pumice fall and/or PDC deposits. The first two tephra deposits are associated with two different caldera-forming eruptions: the (1) Suke caldera deposits that are characterized by a lag breccia lithofacies and (2) Meki caldera eruption, represented by a very thick tephra fall and flow succession with an age of 107.7 ± 8.8 (2σ) ka ($^{40}Ar/^{39}Ar$). This new age of the Meki tephra reveals it to be the youngest caldera-forming eruption identified in the Central MER so far. During the post-caldera volcanism, the BBTM underwent at least 25 moderate-major eruptions sourced from Baricha (9), Bora (3), Oda (8), Werdi (3) and Tullu Moye (2) edifices. The melts that formed these deposits are categorized as comenditic (Tullu Moye) and pantelleritic rhyolites based on the major element glass chemistry. The trace element data indicates that the BBTM pantelleritic tephra are more evolved than those of Aluto volcano located to the south of the study area. The componentry of these deposits reveals a significant variation in pumice, lithics and free mineral content within the deposits. The pumice has a very low percentage of phenocrysts (<10%).

When we consider the BBTM post-caldera phase only, the recurrence rate of the explosive activity from this extended volcanic system is ≥1 eruption per 4000 yrs. This explosive eruption frequency is much lower compared to Aluto and Corbetti, which has been reconstructed from both terrestrial and lacustrine records. The estimated tephra volume for the well exposed units indicates eruption magnitudes pre-dominantly varying from 4 to 5. Only at Tullu Moye deposits of smaller (magnitude 2.5) eruptions were identified in the geological record. For most of the larger eruptions, tephra was dispersed up to 20 km from the volcanic centre suggesting that more than hundred thousand people could be affected by future eruptions of similar magnitude in this area.

Acknowledgements

AT is supported by the F.R.S.-FNRS Aspirant doctoral fund. Several samples and an extensive glass chemistry dataset were collected under the NERC-funded RiftVolc Large Grant (NE/L013649/1) by KF along with others. We would like to thank Tamsin Mather and David Pyle for giving the permission to access the dataset and samples from the RiftVolc project. KF further acknowledges support from F.R.S.-FNRS MIS grant F.4515.20. The iCRAG LA-ICP-MS facility at Trinity College Dublin is supported by SFI award 13/RC/2092. Field work and sample export was kindly permitted by authorities of the Oromia region and Ministry of Mines and Petroleum of Ethiopia, respectively. Professional logistical support was provided by Ethioder Pvt Ltd Co and their drivers. Mathieu Boudin (KIK-IRPA, Institut Royal du Patrimoine Artistique) handled the radiocarbon dating. We thank Thomas Gernon and one anonymous reviewer for detailed and constructive comments which improved the paper.

Reference

Agostini, A., Bonini, M., Corti, G., Sani, F. and Mazzarini, F., 2011. Fault architecture in the Main Ethiopian Rift and comparison with experimental models: implications for rift evolution and Nubia–Somalia kinematics. Earth and Planetary Science Letters, 301(3-4): 479-492.

Albino, F. and Biggs, J., 2021. Magmatic Processes in the East African Rift System: Insights From a 2015–2020 Sentinel-1 InSAR Survey. Geochemistry, Geophysics, Geosystems, 22(3): e2020GC009488.

Albert, P. G., Tomlinson, E. L., Smith, V. C., Di Traglia, F., Pistolesi, M., Morris, A.,Donato, P., De Rosa, R., Sulpizio, R., Keller, J. and Rosi, M., 2017. Glass geochemistry of pyroclastic deposits from the Aeolian Islands in the last 50 ka: a proximal database for tephrochronology. Journal of Volcanology and Geothermal Research, 336: 81-107.

Aravena, A., 2017. Stability of volcanic conduits: Critical mechanical parameters. Il nuovo cimento C, 40(2): 1-9.

Aspinall, W. P., Auker, M., Hincks, T., Mahony, S., Nadim, F., Pooley, J., Sparks, R.S.J. and Syre, E., 2011. Volcano hazard and exposure in GFDRR priority countries and risk mitigation measures. Volcano Risk Study 0100806-00-1-R. Global Facility for disaster Reduction and Recovery, Washington, D.C.

Ayele, A., Teklemariam, M.and Kebede, S., 2002. Geothermal exploration in the Abaya and Tulu Moye-Gedemsa prospects, Main Ethiopian Rift. Geological Survey of Ethiopia, Addis Ababa, 79 pp.

Balestrieri, M. L., Bonini, M., Corti, G., Sani, F. and Philippon, M., 2016. A refinement of the chronology of rift-related faulting in the Broadly Rifted Zone, southern Ethiopia, through apatite fission-track analysis. Tectonophysics, 671: 42-55.

Bastow, I. D., Keir, D. and Daly, E., 2011. The Ethiopia Afar Geoscientific Lithospheric Experiment (EAGLE): Probing the transition from continental rifting to incipient seafloor spreading. Volcanism and evolution of the African lithosphere, 478: 1-26.

Benvenuti, M., Carnicelli, S., Belluomini, G., Dainelli, N., Di Grazia, S., Ferrari, G. A., Lasio, C., Sagri, M., Ventra, D., Atnafu, B. and Kebede, S., 2002. The Ziway–Shala lake basin (main Ethiopian rift, Ethiopia): a revision of basin evolution with special reference to the Late Quaternary. Journal of African Earth Sciences, 35(2): 247-269.

Benvenuti, M., Bonini, M., Tassi, F., Corti, G., Sani, F., Agostini, A., Manetti, P and Vaselli, O., 2013. Holocene lacustrine fluctuations and deep CO2 degassing in the northeastern Lake Langano Basin (Main Ethiopian Rift). Journal of African Earth Sciences, 77: 1-10.

Biggs, J., Bastow, I. D., Keir, D. and Lewi, E., 2011. Pulses of deformation reveal frequently recurring shallow magmatic activity beneath the Main Ethiopian Rift. Geochemistry, Geophysics, Geosystems, 12(9).

Bizouard, H. and Di Paola, G. M., 1978. Mineralogy of the Tullu Moje active volcanic area (Arussi: Ethiopian Rift valley). In Petrology and Geochemistry of Continental Rifts (pp. 87-100). Springer, Dordrecht.

Bonadonna, C., Ernst, G. G. J. and Sparks, R. S. J., 1998. Thickness variations and volume estimates of tephra fall deposits: the importance of particle Reynolds number. Journal of Volcanology and Geothermal Research, 81(3-4): 173-187.

Bonadonna, C. and Houghton, B. F., 2005. Total grain-size distribution and volume of tephra-fall deposits. Bulletin of Volcanology. 67(5): 441-456.

Bronk Ramsey, C., 2009. Bayesian analysis of radiocarbon dates. Radiocarbon 51, 337e360.

Brown, S. K., Crosweller, H. S., Sparks, R. S. J., Cottrell, E., Deligne, N. I., Guerrero, N. O., Hobbs, L., Kiyosugi, K., Loughlin, S.C., Siebert, L. and Takarada, S., 2014. Characterisation of the Quaternary eruption record: analysis of the Large Magnitude

Explosive Volcanic Eruptions (LaMEVE) database. Journal of Applied Volcanology, 3(1): 1-22.

Cas, R., Porritt, L., Pittari, A. and Hayman, P., 2008. A new approach to kimberlite facies terminology using a revised general approach to the nomenclature of all volcanic rocks and deposits: descriptive to genetic. Journal of Volcanology and Geothermal Research, 174(1-3): 226-240.

Calder, E.S., Wagner, K. and Ogburn, S.E., 2015. Volcanic hazard maps. In: Loughlin, S.C., Sparks, R.S.J., Brown, S.K., Jenkins, S.F., Vye-Brown, C. (eds). Global volcanic hazards and risk, Cambridge. Cambridge University Press, 335-342.

Central Statistical Agency of Ethiopia (CSAE), 2007. The 2007 Population and Housing Census of Ethiopia: Statistical Report for Oromiya Region; Part I: Population Size and Characteristics. Report, Addis Ababa, Ethiopia.

Clarke, B., Calder, E. S., Dessalegn, F., Fontijn, K., Cortés, J. A., Naylor, M., Butler, I., Hutchison, W. and Yirgu, G., 2019. Fluidal pyroclasts reveal the intensity of peralkaline rhyolite pumice cone eruptions. Nature communications, 10(1): 1-10.

Clarke, B. A., Tierz, P., Calder, E. S. and Yirgu, G., 2020. Probabilistic volcanic hazard assessment for pyroclastic density currents from pumice cone eruptions at Aluto volcano, Ethiopia. Frontiers in Earth Science, 348.

Daly, E., Keir, D., Ebinger, C. J., Stuart, G. W., Bastow, I. D. and Ayele, A., 2008. Crustal tomographic imaging of a transitional continental rift: the Ethiopian rift. Geophysical Journal International, 172(3): 1033-1048.

Di Paola, G. M., 1972. The Ethiopian Rift Valley (between 7 00′ and 8 40′ lat. north). Bulletin Volcanologique, 36(4): 517-560.

Donovan, A. and Oppenheimer, C., 2012. Governing the lithosphere: insights from Eyjafjallajökull concerning the role of scientists in supporting decision-making on active volcanoes. Journal of Geophysical Research: Solid Earth, 117(B3).

Druitt, T. H., 1985. Vent evolution and lag breccia formation during the Cape Riva eruption of Santorini, Greece. The Journal of Geology, 93(4): 439-454.

Druitt, T. H. and Sparks, R. S. J., 1982. A proximal ignimbrite breccia facies on Santorini, Greece. Journal of Volcanology and Geothermal Research, 13(1-2): 147-171.

Druitt, T. H. and Sparks, R. S. J., 1984. On the formation of calderas during ignimbrite eruptions. Nature, 310(5979): 679-681.

Ebinger, C., 2005. Continental break-up: the East African perspective. Astronomy & Geophysics, 46(2): 2-16.

Ebinger, C. J., Yemane, T., Harding, D. J., Tesfaye, S., Kelley, S. and Rex, D. C., 2000. Rift deflection, migration, and propagation: Linkage of the Ethiopian and Eastern rifts, Africa. Geological Society of America Bulletin, 112(2): 163-176.

Ebinger, C. J. and Casey, M., 2001. Continental breakup in magmatic provinces: An Ethiopian example. Geology, 29(6): 527-530.

Electroconsult (ELC), 1978. Geothermal reconnaissance study of selected sites of the Ethiopian rift system. Geological report, Milano, Italy.

Fierstein, J. and Hildreth, W., 1992. The plinian eruptions of 1912 at Novarupta, Katmai national park, Alaska. Bulletin of Volcanology, 54(8): 646-684.

Fontijn, K., McNamara, K., Tadesse, A. Z., Pyle, D. M., Dessalegn, F., Hutchison, W., Mather, T.A. and Yirgu, G., 2018. Contrasting styles of post-caldera volcanism along the Main Ethiopian Rift: Implications for contemporary volcanic hazards. Journal of Volcanology and Geothermal Research, 356: 90-113.

Froggatt, P. C., 1983. Toward a comprehensive Upper Quaternary tephra and ignimbrite stratigraphy in New Zealand using electron microprobe analysis of glass shards. Quaternary research, 19(2): 188-200.

Gouin, P., 1979. Earthquake history of Ethiopia and the Horn of Africa. IDRC, Ottawa, ON, CA.

Greenfield, T., Keir, D., Kendall, J. M. and Ayele, A., 2019a. Low-frequency earthquakes beneath Tullu Moye volcano, Ethiopia, reveal fluid pulses from shallow magma chamber. Earth and Planetary Science Letters, 526: 115782.

Greenfield, T., Keir, D., Kendall, J. M. and Ayele, A., 2019b. Seismicity of the Bora-Tullu Moye Volcanic Field, 2016–2017. Geochemistry, Geophysics, Geosystems, 20(2): 548-570.

Harangi, S., Molnár, K., Schmitt, A. K., Dunkl, I., Seghedi, I., Novothny, Á., Molnár, M., Kiss, B., Ntaflos, T., Mason, P.R. and Lukács, R., 2020. Fingerprinting the Late Pleistocene tephras of Ciomadul volcano, eastern–central Europe. Journal of Quaternary Science, 35(1-2): 232-244.

Heiken, G. and McCoy Jr, F., 1984. Caldera development during the Minoan eruption, Thira, Cyclades, Greece. Journal of Geophysical Research: Solid Earth, 89(B10): 8441-8462.

Hildreth, W. and Mahood, G. A., 1986. Ring-fracture eruption of the Bishop Tuff. Geological Society of America Bulletin, 97(4): 396-403.

Houghton, B. F. and Wilson, C. J. N., 1989. A vesicularity index for pyroclastic deposits. Bulletin of volcanology, 51(6): 451-462.

Hutchison, W., Fusillo, R., Pyle, D. M., Mather, T. A., Blundy, J. D., Biggs, J., Yirgu, G., Cohen, B.E., Brooker, R.A., Barfod, D.N. and Calvert, A. T., 2016a. A pulse of mid-Pleistocene rift volcanism in Ethiopia at the dawn of modern humans. Nature Communications, 7(1): 1-12.

Hutchison, W., Pyle, D. M., Mather, T. A., Yirgu, G., Biggs, J., Cohen, B. E., Barfod, D.N. and Lewi, E., 2016b. The eruptive history and magmatic evolution of Aluto volcano: new insights into silicic peralkaline volcanism in the Ethiopian rift. Journal of Volcanology and Geothermal Research, 328: 9-33.

Hutchison, W., Biggs, J., Mather, T. A., Pyle, D. M., Lewi, E., Yirgu, G., Caliro, S., Chiodini, G., Clor, L.E. and Fischer, T. P., 2016c. Causes of unrest at silicic calderas in the East African Rift: New constraints from InSAR and soil-gas chemistry at Aluto volcano, Ethiopia. Geochemistry, Geophysics, Geosystems, 17(8): 3008-3030.

Jochum, K. P., Stoll, B., Herwig, K., Willbold, M., Hofmann, A. W., Amini, M., Aurburg, S., Abouchami, W., Hellebrand E. and Raczek, I., 2006. MPI-DING reference glasses for in situ microanalysis: New reference values for element concentrations and isotope ratios. Geochemistry, Geophysics, Geosystems, 7(2).

Jochum, K. P., Weis, U., Stoll, B., Kuzmin, D., Yang, Q., Raczek, I.,Jacobe, D.E, Stracke, A., Birbaum, K., Frick, D.A. and Günther, D., 2011. Determination of reference values for NIST SRM 610–617 glasses following ISO guidelines. Geostandards and Geoanalytical Research, 35(4): 397-429.

Jordan, N. J., Rotolo, S. G., Williams, R., Speranza, F., McIntosh, W. C., Branney, M. J. and Scaillet, S., 2018. Explosive eruptive history of Pantelleria, Italy: Repeated caldera collapse and ignimbrite emplacement at a peralkaline volcano. Journal of Volcanology and Geothermal Research, 349: 47-73.

Kazmin, V. and Berhe, S. M., 1978. Geology and development of the Nazret area. Northern Ethiopian Rift sheet NC37–15, Memoir, 3: 26.

Keir, D., Ebinger, C. J., Stuart, G. W., Daly, E. and Ayele, A., 2006. Strain accommodation by magmatism and faulting as rifting proceeds to breakup: Seismicity of the northern Ethiopian rift. Journal of Geophysical Research: Solid Earth, 111(B5).

Korme, T., Acocella, V. and Abebe, B., 2004. The role of pre-existing structures in the origin, propagation and architecture of faults in the Main Ethiopian Rift. Gondwana Research, 7(2): 467-479.

Le Bas, M. J., Maitre, R. L., Streckeisen, A., Zanettin, B. and IUGS Subcommission on the Systematics of Igneous Rocks, 1986. A chemical classification of volcanic rocks based on the total alkali-silica diagram. Journal of petrology, 27(3): 745-750.

Legros, F., 2000. Minimum volume of a tephra fallout deposit estimated from a single isopach. Journal of Volcanology and Geothermal Research, 96(1-2): 25-32.

Le Turdu, C., Tiercelin, J. J., Gibert, E., Travi, Y., Lezzar, K. E., Richert, J. P., Massault, M., Gesse, F., Bonnefille, R., Decobert, M. and Gensous, B., 1999. The Ziway–Shala lake basin system, Main Ethiopian Rift: influence of volcanism, tectonics, and climatic forcing on basin formation and sedimentation. Palaeogeography, Palaeoclimatology, Palaeoecology, 150(3-4): 135-177.

Lipman, P. W., 1984. The roots of ash flow calderas in western North America: windows into the tops of granitic batholiths. Journal of Geophysical Research: Solid Earth, 89(B10): 8801-8841.

Loughlin, S. C., Sparks, R. S. J., Sparks, S., Brown, S. K., Jenkins, S. F. and Vye-Brown, C., 2015. Global volcanic hazards and risk. Cambridge University Press.

Lowe, D. J., 2011. Tephrochronology and its application: a review. Quaternary Geochronology, 6(2): 107-153.

Macdonald, R., 1974. Nomenclature and petrochemistry of the peralkaline oversaturated extrusive rocks. Bulletin volcanologique, 38(2): 498-516.

Mamo, T., 2002. Surface hydrothermal alteration in the Tullu Moye area, Lakes district rift, Ethiopia. Geological Survey of Ethiopia, Addis Ababa, 7 pp.

Martin-Jones, C. M., Lane, C. S., Pearce, N. J., Smith, V. C., Lamb, H. F., Schaebitz, F., Viehberg, F., Brown, M.C., Frank, U. and Asrat, A., 2017. Recurrent explosive eruptions from a high-risk Main Ethiopian Rift volcano throughout the Holocene. Geology, 45(12): 1127-1130.

McNamara, K., Cashman, K. V., Rust, A. C., Fontijn, K., Chalié, F., Tomlinson, E. L. and Yirgu, G., 2018. Using lake sediment cores to improve records of volcanism at Aluto volcano in the Main Ethiopian Rift. Geochemistry, Geophysics, Geosystems, 19(9): 3164-3188.

Mulugeta, B. D., Fujimitsu, Y., Nishijima, J. and Saibi, H., 2021. Interpretation of gravity data to delineate the subsurface structures and reservoir geometry of the Aluto–Langano geothermal field, Ethiopia. Geothermics, 94: 102093.

Niespolo, E. M., Rutte, D., Deino, A. L. and Renne, P. R., 2017. Intercalibration and age of the Alder Creek sanidine 40Ar/39Ar standard. Quaternary Geochronology, 39: 205-213.

Peccerillo, A., Barberio, M. R., Yirgu, G., Ayalew, D., Barbieri and Wu, T. W., 2003. Relationships between mafic and peralkaline silicic magmatism in continental rift settings: a petrological, geochemical and isotopic study of the Gedemsa volcano, central Ethiopian rift. Journal of Petrology, 44(11): 2003-2032.

Polacci, M., Pioli, L. and Rosi, M., 2003. The Plinian phase of the Campanian Ignimbrite eruption (Phlegrean Fields, Italy): evidence from density measurements and textural characterization of pumice. Bulletin of Volcanology, 65(6): 418-432.

Pyle, D. M., 1989. The thickness, volume and grainsize of tephra fall deposits. Bulletin of Volcanology, 51(1): 1-15.

Pyle, D. M., 2015. Sizes of volcanic eruptions. In The encyclopedia of volcanoes (pp. 257-264). Academic Press.

Rapprich, V., Žáček, V., Verner, K., Erban, V., Goslar, T., Bekele, Y., Legesa, F., Hroch, T. and Hejtmánková, P., 2016. Wendo Koshe Pumice: The latest Holocene silicic explosive eruption product of the Corbetti volcanic system (southern Ethiopia). Journal of Volcanology and Geothermal Research, 310: 159-171.

Reimer, P. J., Austin, W. E., Bard, E., Bayliss, A., Blackwell, P. G., Ramsey, C. B., Butzin, M., Cheng, H., Edwards, R.L., Friedrich, M. and Talamo, S., 2020. The IntCal20 Northern Hemisphere radiocarbon age calibration curve (0–55 cal kBP). Radiocarbon, 62(4): 725-757.

Renne, P. R., Balco, G., Ludwig, K. R., Mundil, R. and Min, K., 2011. Response to the comment by WH Schwarz et al. on “Joint determination of 40K decay constants and 40Ar∗/40K for the Fish Canyon sanidine standard, and improved accuracy for 40Ar/39Ar geochronology” by PR Renne et al.(2010). Geochimica et Cosmochimica Acta, 75(17): 5097-5100.

Roduit, N., 2019. Image analysis toolbox for measuring and quantifying components of high-definition images, JMicroVision: Version 1.3.1. https://jmicrovision.github.io (accessed 10 August 2020).

Rooney, T., Furman, T., Bastow, I., Ayalew, D. and Yirgu, G., 2007. Lithospheric modification during crustal extension in the Main Ethiopian Rift. Journal of Geophysical Research: Solid Earth, 112(B10).

Schneider, C.A., Rasband, W.S. and Eliceiri, K. W., 2012. NIH Image to ImageJ: 25 years of image analysis. Nature methods, 9(7): 671-675.

Seggiaro, R. E., Guzmán, S. R. and Martí, J., 2019. Dynamics of caldera collapse during the Coranzulí eruption (6.6 Ma)(Central Andes, Argentina). Journal of Volcanology and Geothermal Research, 374: 1-12.

Siegburg, M., Gernon, T. M., Bull, J. M., Keir, D., Barfod, D. N., Taylor, R. N., Abebe, B. and Ayele, A., 2018. Geological evolution of the Boset-Bericha volcanic complex, Main Ethiopian Rift: 40Ar/39Ar evidence for episodic Pleistocene to Holocene volcanism. Journal of Volcanology and Geothermal Research, 351: 115-133.

Smith, V. C., Pearce, N. J., Matthews, N. E., Westgate, J. A., Petraglia, M. D., Haslam, M., Lane, C.S., Korisettar, R. and Pal, J. N., 2011. Geochemical fingerprinting of the widespread Toba tephra using biotite compositions. Quaternary International, 246(1-2): 97-104.

Spence, R. J. S., Kelman, I., Baxter, P. J., Zuccaro, G. and Petrazzuoli, S., 2005. Residential building and occupant vulnerability to tephra fall. Natural Hazards and Earth System Sciences, 5(4): 477-494.

Teklemariam, M., Battaglia, S., Gianelli, G. and Ruggieri, G., 1996. Hydrothermal alteration in the Aluto-Langano geothermal field, Ethiopia. Geothermics, 25(6): 679-702.

Tierz, P., Clarke, B., Calder, E. S., Dessalegn, F., Lewi, E., Yirgu, G., Fontijn, K., Crummy, J.M., Bekele, Y. and Loughlin, S. C., 2020. Event trees and epistemic uncertainty in long-term volcanic hazard assessment of rift volcanoes: The example of Aluto (Central Ethiopia). Geochemistry, Geophysics, Geosystems, 21(10).

United Nations Development Programme (UNDP), 1973. Geology, geochemistry and hydrology of hot springs of the East African Rift system within Ethiopia. In Investigation of geothermal resources for power development (Tech. Rep. DP/SF/UN 116, 275 pp.). New York, NY: United Nations.

Varet, J. and Birba, E. Tullu Moye Geothermal Project (Oromia, Ethiopia). In proceedings, 7th African Rift Geothermal Conference, Kigali, Rwanda 31st October – 2nd November 2018, 15 pp.

Walker, G. P., 1985. Origin of coarse lithic breccias near ignimbrite source vents. Journal of Volcanology and Geothermal Research, 25(1-2): 157-171.

Wilson, TM, Stewart, C., Sword-Daniels, V., Leonard, GS, Johnston, DM, Cole, JW, Wardman, J., Wilson, G. and Barnard, ST., 2012. Volcanic ash impacts on critical infrastructure. Physics and Chemistry of the Earth, Parts A / B / C, 45: 5-23.

WoldeGabriel, G., Aronson, J. L. and Walter, R. C., 1990. Geology, geochronology, and rift basin development in the central sector of the Main Ethiopia Rift. Geological Society of America Bulletin, 102(4): 439-458.

Figures

Figure 1: Overview map of the MER and its main volcanic and tectonic features. The location of the BBTM volcanic system is indicated by a dashed rectangle (for a more detailed view, see Fig.2a). Along-rift volcanoes that are considered to be active, with eruptions in the Holocene, are indicated by a red triangle. BJVF: Butajira Volcanic Field; DZVF: Debre Zeyt Volcanic Field, are mainly basaltic lava and scoria cones located at the MER western margin. MER faults after Agostini et al. (2011). Inset shows location of the main map (solid rectangle). The Kenyan rift (KR) is connected to the MER by a broadly rifted zone with little to no surface expression of magmatism. The MER progresses northwards in the Afar Depression forming a triple junction with the Gulf of Aden (GA) and Red Sea (RS) rifts.

Figure 2: (A) Map of Bora-Baricha-Tullu Moye volcanic complex showing the distribution of different volcanic centres, visited outcrops (the most important of which are labelled with three digits referring to their MER outcrops name; SM-3) and shallow drill well sites (see Fig. 2b; after Ayele et al. 2002). Some outcrops indicated on this figure are the same as those in Fontijn et al. (2018). The Werdi vent (spelled also Werdia) is locally also known as Dima. The extent of the A-A’ profile (Fig. 2b) is indicated by two crosss. (B) West-East (A-A’) cross

section showing the sub-surface stratigraphy of BBTM from shallow drill-cores (data from Ayele et al. 2002). The elevation scale on the y axis represents the well stratigraphy; topography is two times vertically exaggerated.

Figure 3: Tephrostratigraphic framework of the BBTM volcanic complex. (A) Baricha, Meki and Suke. (B) Bora, Oda, Werdi and Tullu Moye. Correlations between the different sections are based on stratigraphic position, physical characteristics, petrography and glass chemical composition of the deposits. The relative geographic location in the volcanic system and the scale of the stratigraphic sections are indicated on this figure and can be seen in Fig. 2. The symbols used on geochemical plots of each BBTM unit (Figs. 6-8) are shown for cross-reference.

Figure 4: Field photographs of some of the BBTM pyroclastic deposits. The representative pictures show type sections for Suke (A), Meki (B), Baricha (C), Bora (D), Werdi (E), Oda (F) and Tullu Moye (G) deposits. The symbols are cross referenced to Figure 2 (stratigraphy) and Figures 6-8 (geochemistry).

Figure 5: Componentry and petrography of representative BBTM deposits of (A) Meki, (B) Bora, (C) Werdi, (D) Baricha, (E) Oda and (F) Tullu Moye. For each sample, representative photos illustrating the componentry (left) and petrography (right) are shown, with quantitative results presented on a bar and pie chart respectively. The photos are taken using a stereo zoom and optical petrographic microscope in plane polarised light.

Figure 6: BBTM silicic tephra classification based on major element (wt%) glass composition following (A) Le Bas et al. (1986) and (B) Macdonald (1974). The comparative glass chemistry data for Aluto, Corbetti and Gedemsa volcanoes (dashed lines) are from Fontijn et al. (2018), Martin-Jones et al. (2017) and McNamara et al. (2018).

Figure 7: Bivariate major element (wt%) plots of the BBTM silicic tephra glass compositions. The dashed lines on the diagrams indicate the range of compositions of Aluto, Corbetti and Gedemsa tephra from Fontijn et al. (2018), Martin-Jones et al. (2017) and McNamara et al. (2018). Symbols and colours are the same as in Figure 6.

Figure 8: BBTM tephra trace element (ppm) bivariate and ratio plots. The red dashed line shows the compositional range of Aluto tephra (from McNamara et al. 2018). Symbols and colours are the same as in Figure 6.

Figure 9: Isopach maps (contours in m) for the four major fall deposits from Baricha and Bora, each identified in at least 4 different locations. The minimum (bulk deposit) volume and unit names are indicated on the figures. Volumes are calculated using the Pyle (1989) method for Ba-P4 and Ba-P5, and the Legros (2000) method for Ba-P7 and Bo-P2. Dashed isopach lines are used instead of solid lines where there is great uncertainty in the shape of the contour due to data lack of exposure. The source volcanic centre is indicated by a red triangle and data points by annotated circles.

Tables

Table 1: Compilation of new and existing BBTM age constraints. The $^{40}Ar/^{39}Ar$ ages are quoted with 2σ standard error. Radiocarbon dates were calibrated in OxCal v.4.4 (Bronk Ramsey 2009) using the IntCal20 calibration curve (Reimer et al. 2020).

Table 2: Synoptic overview of all BBTM pyroclastic deposits that were identified in multiple outcrops, with a description of their field appearance and laboratory-based observations that have helped establishing correlations between sections (Fig. 3). The major deposits are described in more detail in the text. Mineral abbreviations: alkali feldspar (Kfs), aenigmatite

(Ang), feldspar (Fs), pyroxene (Px), orthopyroxene (Opx), clinopyroxene (Cpx), amphibole (Amp). Th: thickness.

Table 3: Glass major (wt%) and trace (ppm) element composition of BBTM tephra units. Presented data are average compositions (1 sigma standard deviation in brackets) of one representative sample for each unit. The full data set is provided in supplementary material (SM-2 and SM-5). The analysed number of spots per sample for major (n) and trace (N) elements are indicated.

Supplementary Information

Supplementary material 1 (SM-1): SEM-BSE images and EDS spectra on selected points on two BBTM representative samples (MER201H and MER201A).

- **Figure SM-1.1**: (A) BSE image of pumice sample MER201H. (B & C) Glass semi-quantitative EDS spectra for sample spots indicated on the BSE image.
- **Figure SM-1.2**: (A) BSE image of pumice sample MER201A collected from Baricha deposit Ba-P3. (B-D) Semi-quantitative EDS spectra for sample spots indicated on the BSE image of (B) an ilmenite inclusion, (C) a glass rim and (D) an alkali feldspar.

Supplementary material 2 (SM-2): BBTM glass major element dataset analysed by EPMA.

Supplementary material 3 (SM-3): Outcrop locations and names.

Supplementary material 4 (SM-4): BBTM tephra componentry and petrography dataset.

Supplementary material 5 (SM-5): BBTM glass trace element dataset analysed by LA-ICP-MS.

Supplementary material 6 (SM-6): Tephra volume and magnitude estimates of major BBTM explosive eruptions.

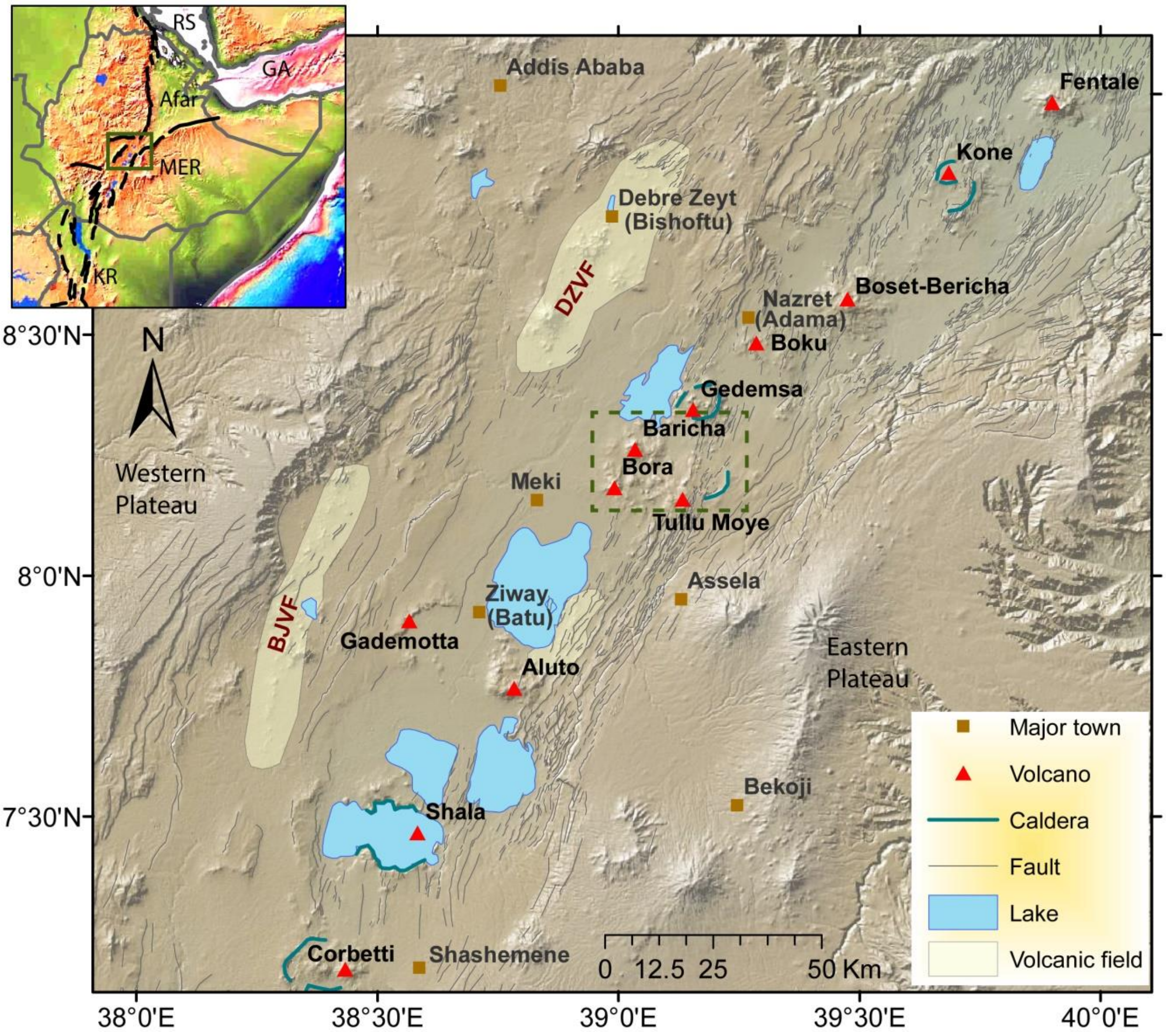

RS
GA
Afar
MER
KR
N
Western Plateau
Eastern Plateau
Addis Ababa
Fentale
Kone
Debre Zeyt (Bishoftu)
DZVF
Boset-Bericha
Nazret (Adama)
Boku
Gedemsa
Baricha
Bora
Meki
Tullu Moye
Assela
Ziway (Batu)
Gademotta
BJVF
Aluto
Bekoji
Shala
Corbetti
Shashemene
0 12.5 25 50 Km
Major town
Volcano
Caldera
Fault
Lake
Volcanic field
8°30'N
8°0'N
7°30'N
38°0'E
38°30'E
39°0'E
39°30'E
40°0'E

Figure 1

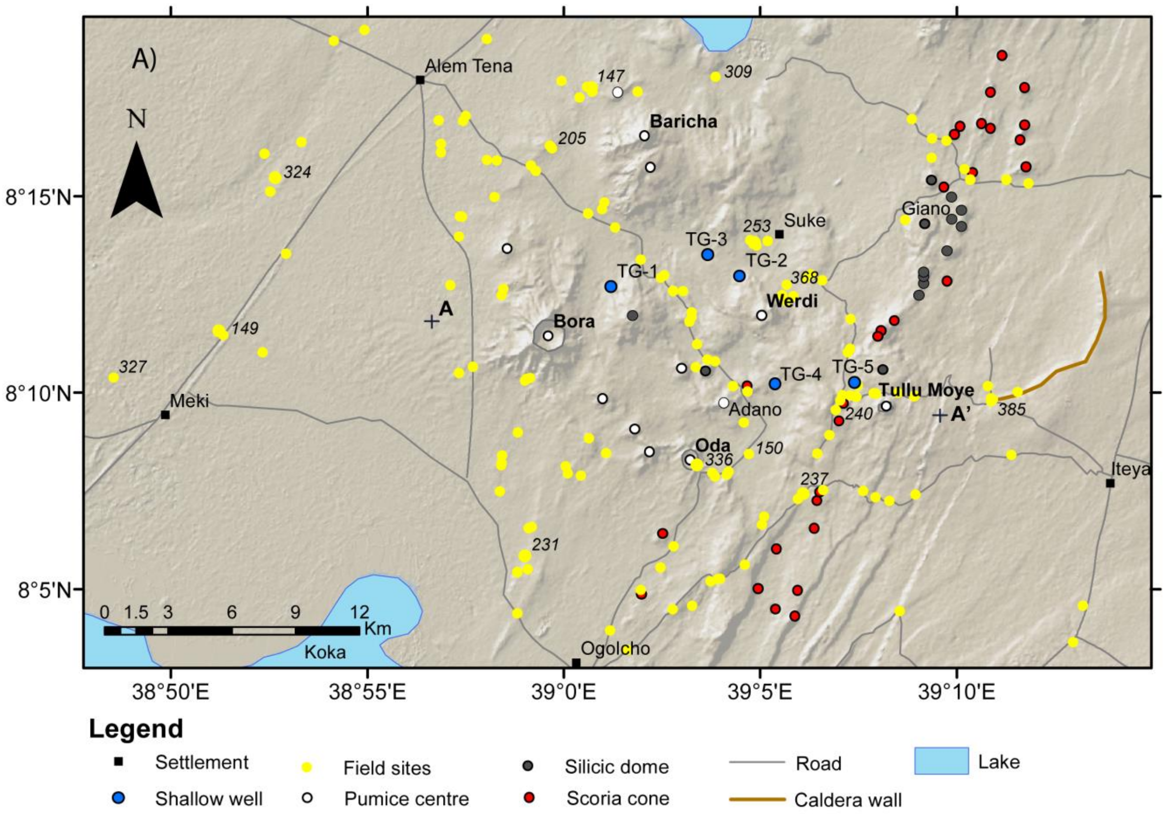
A)
N
Alem Tena
Baricha
Suke
Giano
Werdi
Bora
Tullu Moye
Adano
Oda
Meki
Iteya
Ogolcho
Koka
TG-1
TG-2
TG-3
TG-4
TG-5
A
A'
147
309
205
324
253
368
149
327
240
385
150
336
237
231
0 1.5 3 6 9 12 Km
8°15'N
8°10'N
8°5'N
38°50'E
38°55'E
39°0'E
39°5'E
39°10'E
Legend
Settlement
Shallow well
Field sites
Pumice centre
Silicic dome
Scoria cone
Road
Caldera wall
Lake

Figure 2a

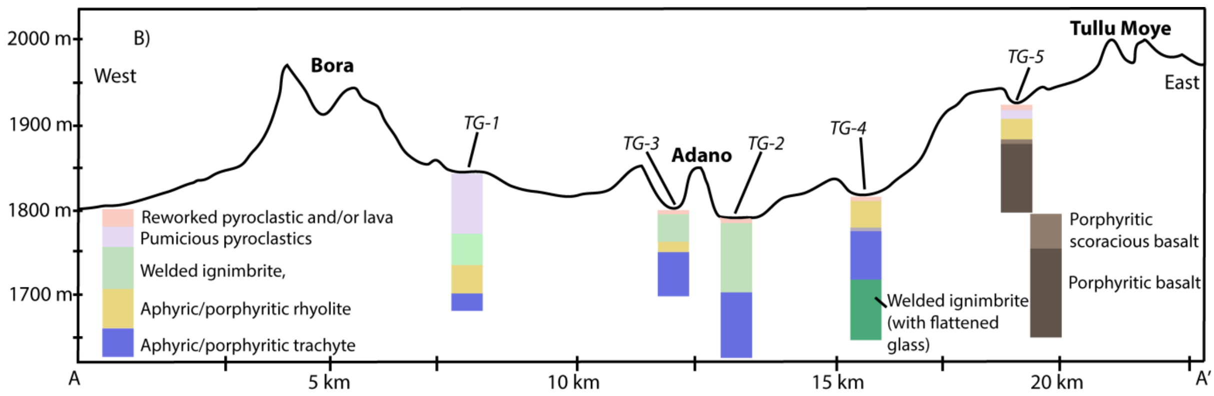

B)
West
Bora
Tullu Moye
East
2000 m
1900 m
1800 m
1700 m
TG-1
TG-3
Adano
TG-2
TG-4
TG-5
Reworked pyroclastic and/or lava
Pumicious pyroclastics
Welded ignimbrite,
Aphyric/porphyritic rhyolite
Aphyric/porphyritic trachyte
Welded ignimbrite (with flattened glass)
Porphyritic scoracious basalt
Porphyritic basalt
A
5 km
10 km
15 km
20 km
A'

Figure 2b

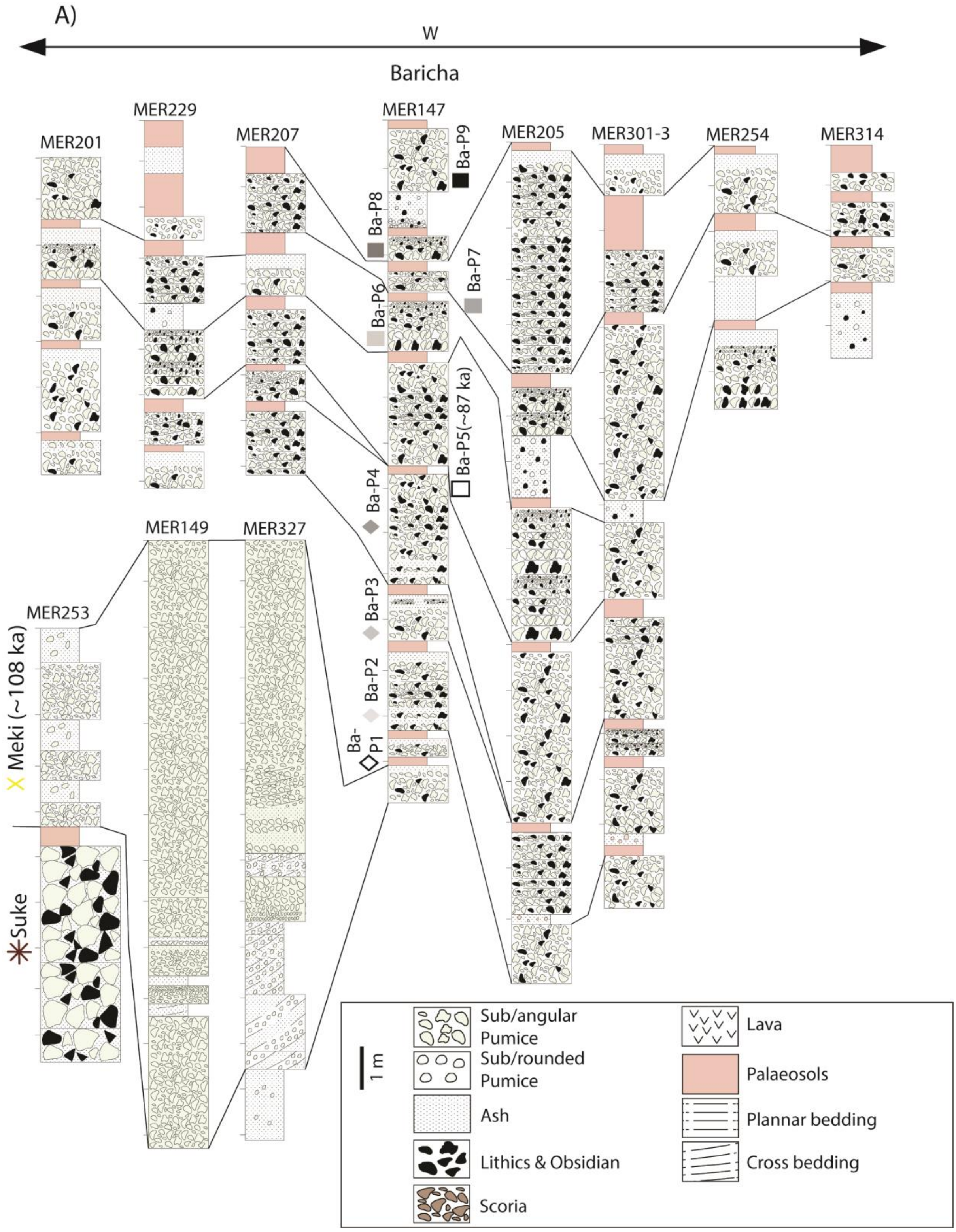

A)
W
Baricha
MER201
MER229
MER207
MER147
MER205
MER301-3
MER254
MER314
Ba-P9
Ba-P8
Ba-P7
Ba-P6
Ba-P5(~87 ka)
Ba-P4
Ba-P3
Ba-P2
Ba-P1
MER149
MER327
MER253
Meki (~108 ka)
Suke
1 m
Sub/angular Pumice
Sub/rounded Pumice
Ash
Lithics & Obsidian
Scoria
Lava
Palaeosols
Plannar bedding
Cross bedding

Figure 3a

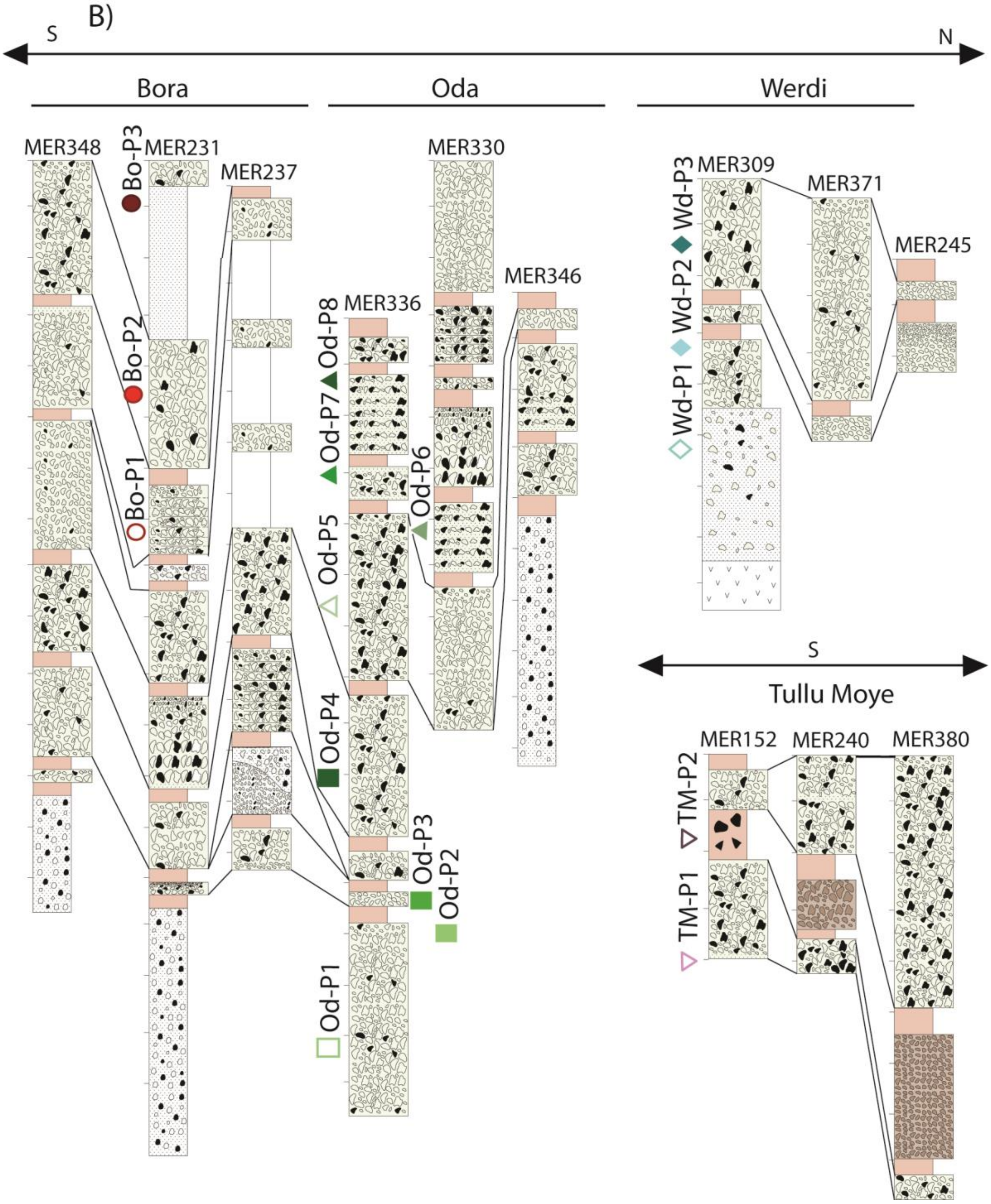
B)
S
N
Bora
Oda
Werdi
MER348
MER231
MER237
MER330
MER336
MER346
MER309
MER371
MER245
Bo-P3
Bo-P2
Bo-P1
Od-P8
Od-P7
Od-P6
Od-P5
Od-P4
Od-P3
Od-P2
Od-P1
Wd-P3
Wd-P2
Wd-P1
S
Tullu Moye
MER152
MER240
MER380
TM-P2
TM-P1

Figure 3b

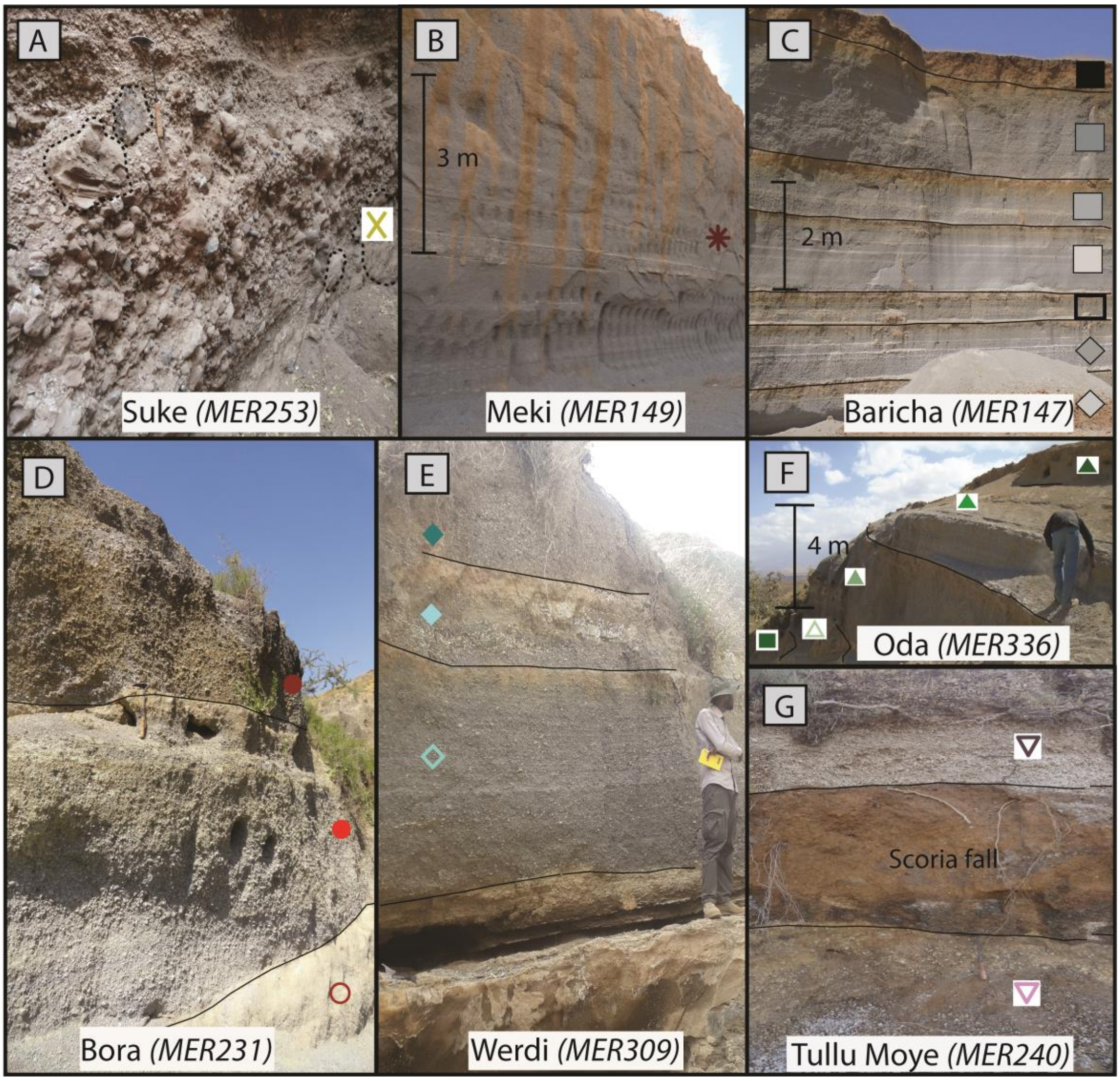
A
Suke (MER253)
B
3 m
Meki (MER149)
C
2 m
Baricha (MER147)
D
Bora (MER231)
E
Werdi (MER309)
F
4 m
Oda (MER336)
G
Scoria fall
Tullu Moye (MER240)

Figure 4

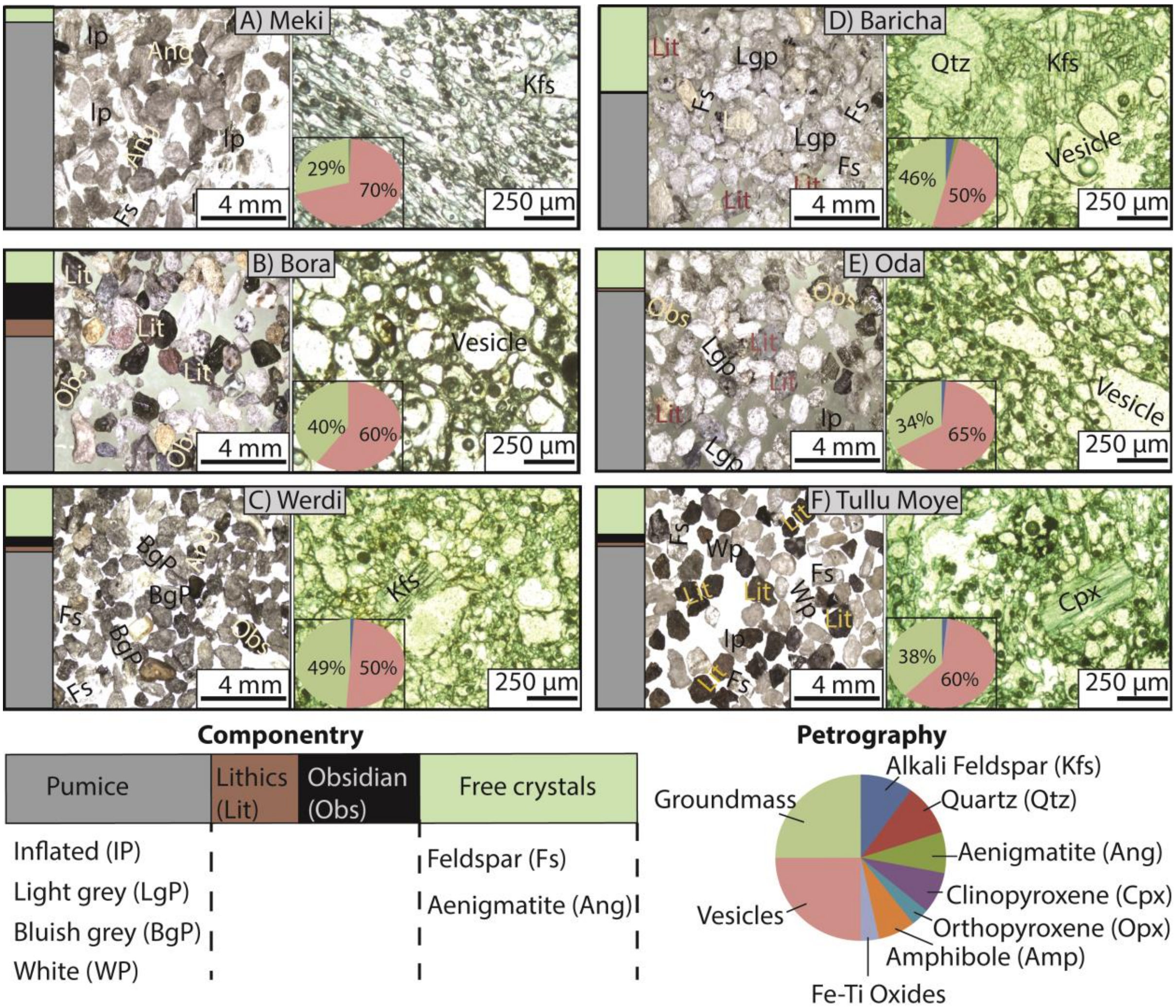
A) Meki
B) Bora
C) Werdi
D) Baricha
E) Oda
F) Tullu Moye
4 mm
250 µm
29%
70%
40%
60%
49%
50%
46%
50%
34%
65%
38%
60%
Componentry
Pumice
Lithics (Lit)
Obsidian (Obs)
Free crystals
Inflated (IP)
Light grey (LgP)
Bluish grey (BgP)
White (WP)
Feldspar (Fs)
Aenigmatite (Ang)
Petrography
Groundmass
Vesicles
Alkali Feldspar (Kfs)
Quartz (Qtz)
Aenigmatite (Ang)
Clinopyroxene (Cpx)
Orthopyroxene (Opx)
Amphibole (Amp)
Fe-Ti Oxides

Figure 5

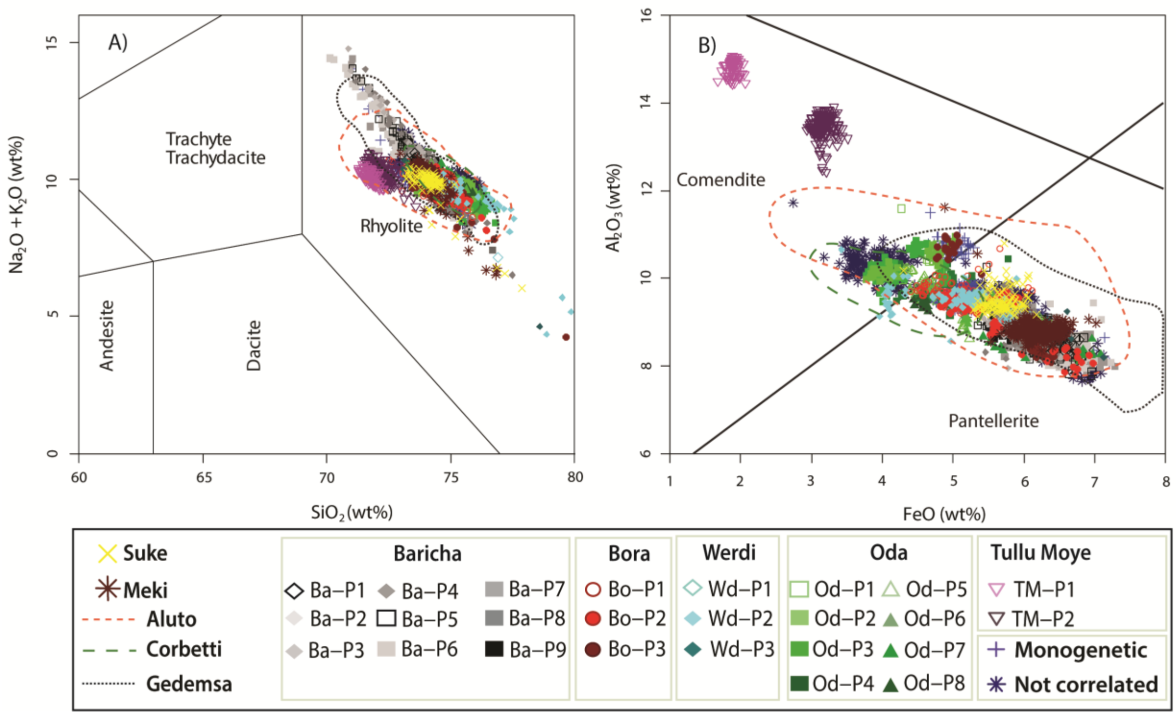
A)
Trachyte
Trachydacite
Rhyolite
Andesite
Dacite
$Na_2O + K_2O$ (wt%)
SiO_2 (wt%)
B)
Comendite
Pantellerite
Al_2O_3 (wt%)
FeO (wt%)
Suke
Meki
Aluto
Corbetti
Gedemsa
Baricha
Ba–P1
Ba–P2
Ba–P3
Ba–P4
Ba–P5
Ba–P6
Ba–P7
Ba–P8
Ba–P9
Bora
Bo–P1
Bo–P2
Bo–P3
Werdi
Wd–P1
Wd–P2
Wd–P3
Oda
Od–P1
Od–P2
Od–P3
Od–P4
Od–P5
Od–P6
Od–P7
Od–P8
Tullu Moye
TM–P1
TM–P2
Monogenetic
Not correlated

Figure 6

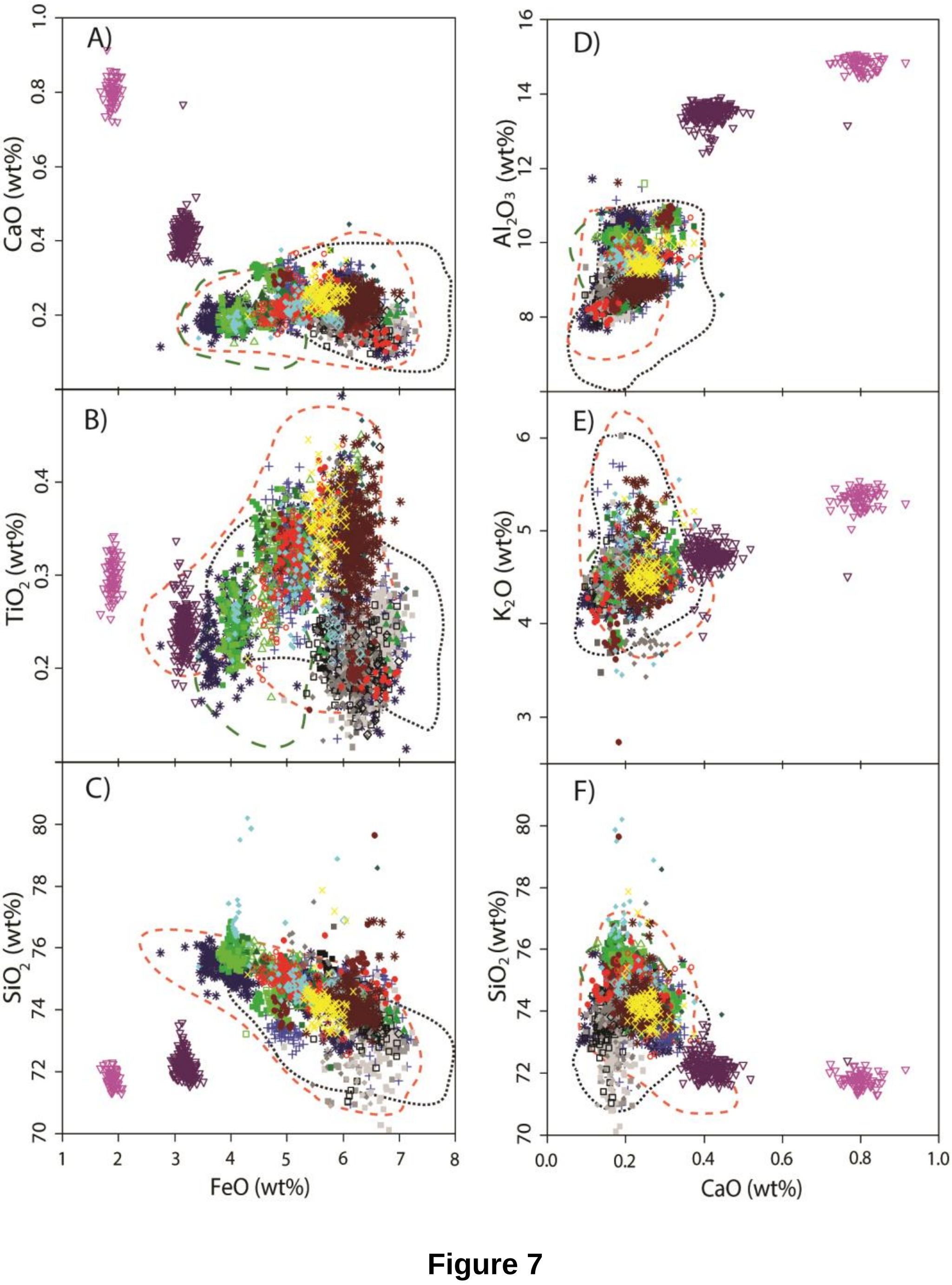

Figure 7

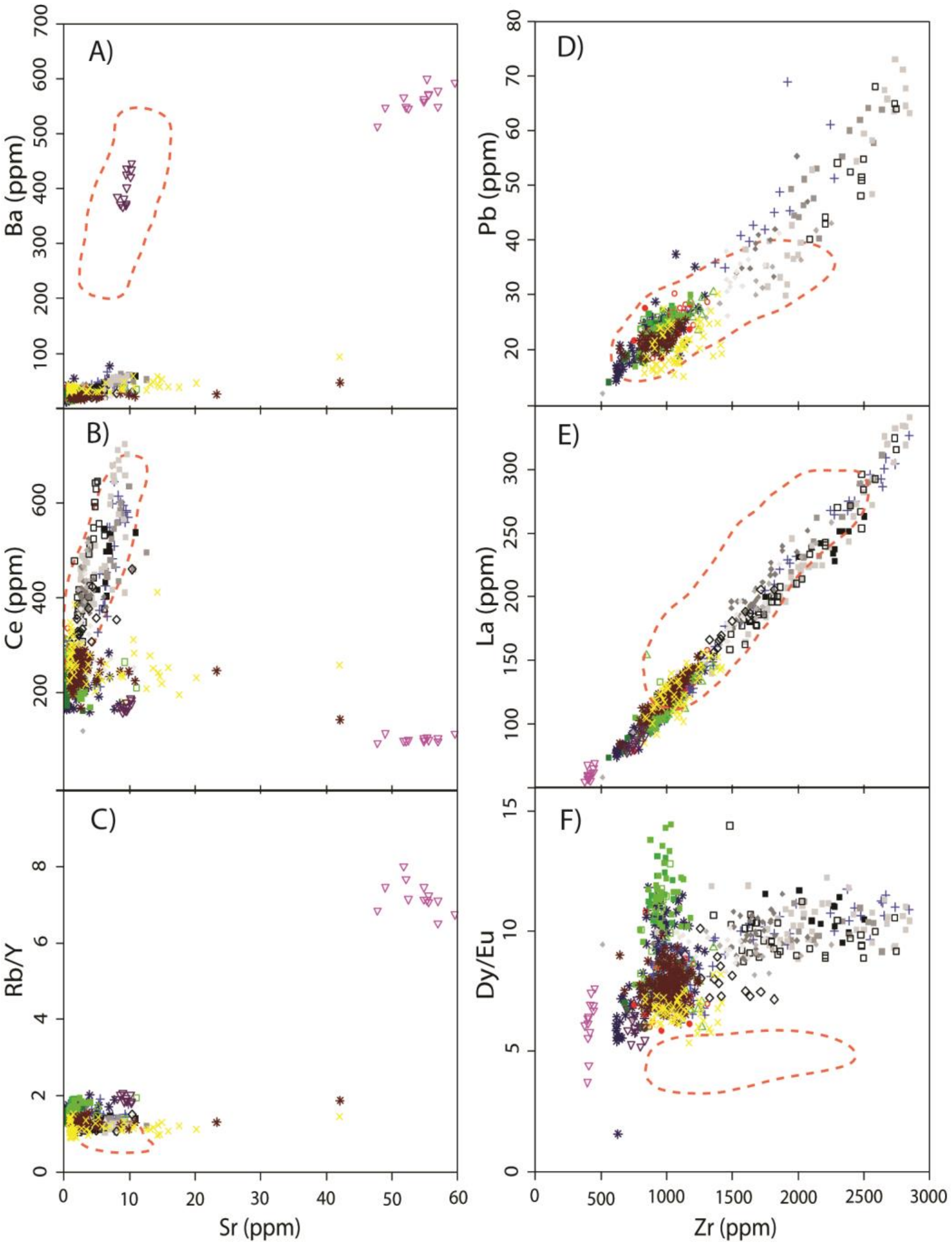

Figure 8

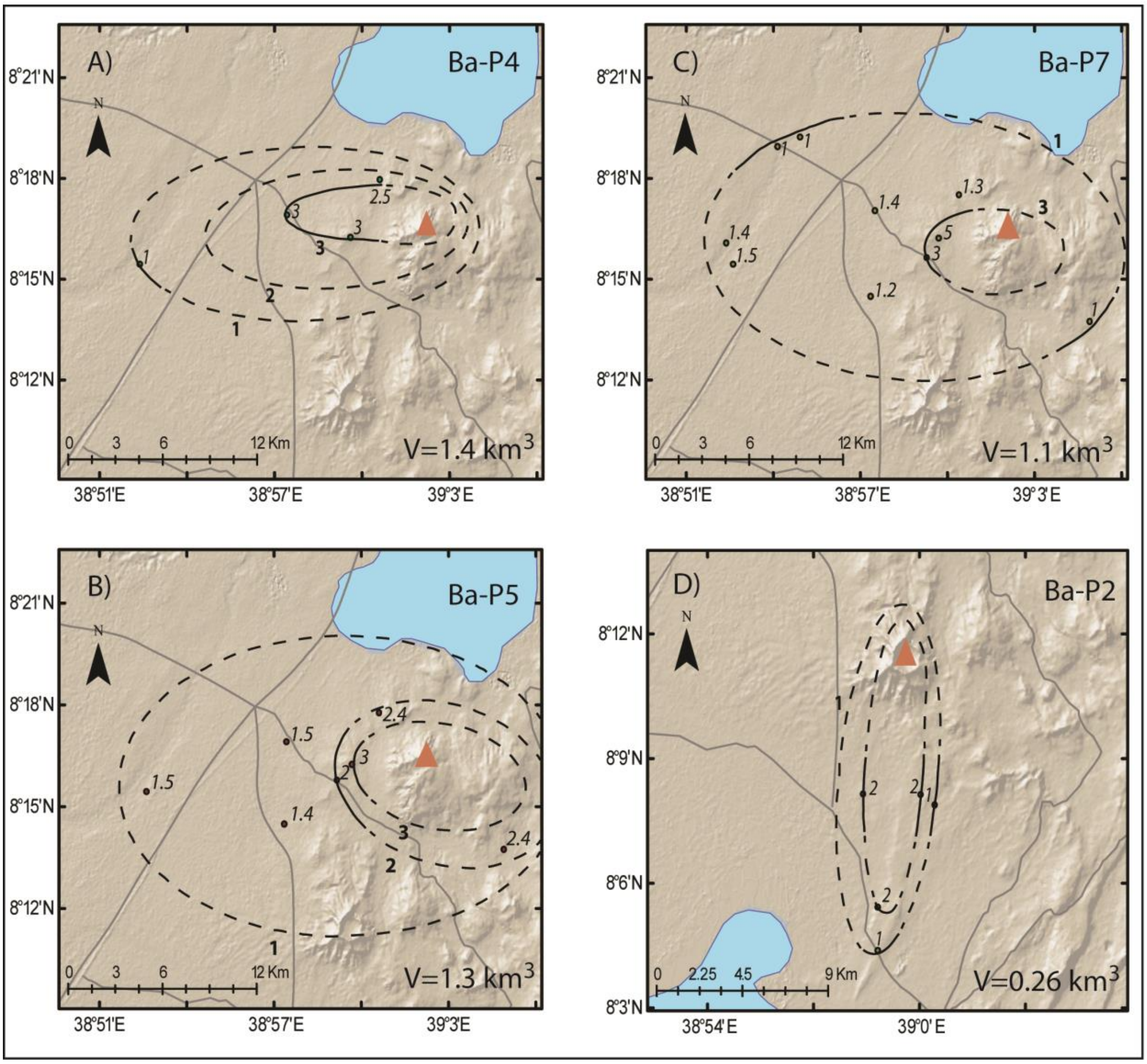
A)
Ba-P4
V=1.4 km3
B)
Ba-P5
V=1.3 km3
C)
Ba-P7
V=1.1 km3
D)
Ba-P2
V=0.26 km3
8°21'N
8°18'N
8°15'N
8°12'N
8°9'N
8°6'N
8°3'N
38°51'E
38°57'E
39°3'E
38°54'E
39°0'E
0 3 6 12 Km
0 2.25 4.5 9 Km

Figure 9

Table 1

Volcanic centre	Sample code	Location		Rock type	Method	Age	Additional note
		Lat	Long				
Unknown	BT-108	Unknown		Obsidian lava	K-Ar	1.58 ± 0.2 Ma	WoldeGabriel et al. (1990)
BBTM	MER149A	8.19	38.85	Tephra	$^{40}Ar/^{39}Ar$ (sanidine)	107.7 ± 8.8 ka	This study
Baricha	MER147-2D	8.29	39	Tephra	$^{40}Ar/^{39}Ar$ (sanidine)	87 ± 16 ka	This study
Baricha	MER308	8.23	39.02	Tephra	^{14}C (charcoal)	1190 ± 36 cal yrs BP	This study

Table 2

Source	Unit	Age	Deposit appearance	Interpretation	Componentry (average of grain size fraction <4 mm unless otherwise indicated)	Petrography	Glass composition	Magnitude
BBTM	**Suke**		Max. Th: 6 m, very poorly sorted, clast-supported, contains bombs and blocks (max. 1 m)	PDC (ignimbrite/lag breccia)	Microvesicular pumice Lava and glassy obsidian lithics	<1% (Ang)	Pantellerite	Caldera forming
BBTM	**Meki**	108±8 ka	Max. Th: >20 m. Top and bottom is massive, well-sorted pumice lapilli breccia with expanded pumice. The middle part is an alternation of poorly and well sorted pumice lapilli breccia beds. The poorly sorted layers have no consistent local thickness, and show mm-scale low-angle cross bedding, and sub-horizontal laminations of poorly sorted and sub-rounded pumice lapilli in fine ash	Sequence of tephra fall (bottom), PDC (middle) and tephra fall (top)	45-90% microvesicular & ≤40% expanded pumice 5-20% free crystals (Fs & Ang) No lithics	70-75% vesicles <1% phenocrysts (Kfs, Ang) Microlite-poor groundmass	Pantellerite	Caldera forming
Baricha	**Ba-P1**		Max. Th: 37 cm. Crudely bedded, well sorted and poorly preserved pumice lapilli	Tephra fall	100% microvesicular pumice		Pantellerite	

		breccia					
Ba-P2		Max. Th: 185 cm. Sub-parallel to low angle cross-bedded units of medium ash and crystal-rich lapilli in bottom third. Dm-scale bedded, well sorted lapilli breccia in the middle and upper portions.	PDC; Tephra fall	60% microvesicular & 2% expanded pumice 30% free crystals (Fs/Qtz, Ang/Amp/Px) 5% lithics (lava & glassy obsidian)		Pantellerite	
Ba-P3		Max. Th: 3 m. Bottom 5-10 cm is fine indurated ash with accretionary lapilli. The rest is light grey pumice lapilli breccia, well sorted, massive to cm-scale crudely bedded with occasional pumice bombs (~15 cm)	Tephra fall	80-90% microvesicular pumice ≤20% free crystals (Fs, Ang & Px) <1% crystal-rich obsidian	65% vesicles 6% phenocrysts (Kfs, Ang, Opx) Glassy groundmass	Pantellerite	4.1
Ba-P4		Max. Th: 2.5 m. Cm-scale fine pumice lapilli interbedded with yellowish ash beds at the base. Massive well-sorted pumice lapilli breccia with occasional pumice bombs	Tephra fall	45-75% microvesicular, <5% expanded & ≤1% tube pumice 10-35% free crystals (Fs, Ang & Fe-Ti Oxides) ≤10% lithics (crystal-rich obsidian, lava & ignimbrite)	65% vesicles <1% phenocrysts (Kfs, Ang) microlite-poor groundmass	Pantellerite	5.1
Ba-P5	87 ± 16 ka	Max. Th: 2.5 m. Massive to cm-to-dm scale crudely bedded well-sorted pumice lapilli breccia	Tephra fall	55-75% microvesicular, ≤20% expanded & ≤1% tube pumice 5-40% free crystals (Fs, Ang/Px/Amp & Fe-Ti Oxides)	50-65% vesicles <10% phenocrysts (Kfs, Ang, Amp, Opx)	Pantellerite	5.1

				≤5% lithics (crystal-rich obsidian, lava & ignimbrite) ≤15% obsidian	Glassy groundmass		
Ba-P6		Max. Th: 4 m. Multiple horizons of normally graded and well-sorted pumice lapilli breccia	Tephra fall	50-70% microvesicular & <10% expanded pumice 30% free crystals (Fs, Ang/Amp & Fe-Ti Oxides) ≤2% lithics (crystal-rich obsidian, lava & ignimbrite) ≤5% obsidian	50% vesicles <10% phenocrysts (Kfs, Ang, Amp) Glassy groundmass	Pantellerite	4.8
Ba-P7		Max. Th: 5 m. Dm-scale crudely bedded, overall normally graded, and poorly sorted pumice lapilli breccia with some pumice bombs (10-15 cm)	Tephra fall	65-85% microvesicular, ≤2% expanded & ≤2% tube pumice 5-30% free crystals (Fs, Ang & Fe-Ti Oxides) ≤2% lithics (crystal rich obsidian, lava & ignimbrite) ≤10% glassy obsidian	50-55% vesicles <1% phenocrysts (Kfs & Ang) Glassy groundmass	Pantellerite	5
Ba-P8		Max. Th: 80 cm. Poorly preserved, highly altered orange-stained pumice lapilli breccia, well sorted with diffuse normal grading	Tephra fall	75% microvesicular & <5% expanded pumice <20% free crystals (Fs, Ang) <5% crystal-rich obsidian lithics	65% vesicles 6% phenocrysts (Kfs & Ang) Glassy groundmass	Pantellerite	
Ba-P9	1190 ± 36 cal yr BP	Max. Th: 2.5 m. Cream-coloured, matrix-supported and undulated beds in the	PDC; Tephra fall	80-100% microvesicular <20% free crystals (Fs/Qtz, Ang/Amp/Px)		Pantellerite	

		bottom half. Parallel bedded, well-sorted pumice lapilli breccia at the top		<1% crystal-rich obsidian			
Oda	**Od-P1**	Max. Th: 4 m. Massive to crudely bedded, poorly sorted pumice lapilli breccia with occasional pumice bombs (3.5 cm)	Tephra fall	100% microvesicular	50% vesicles <3% phenocrysts (Kfs, Ang & Cpx) Glassy groundmass	Pantellerite-Comendite	
	Od-P2	Max. Th: 30 cm. Poorly sorted coarse pumice lapilli breccia with massive to diffuse normal grading	Tephra fall	75-80% microvesicula, 1% tube & ≤1% expanded pumice ≤10% free crystals (Fs/Qtz & Fe-Ti oxides) ≤2% lithics (hydr. altered lava, glassy obsidian & ignimbrite) ≤10% obsidian		Pantellerite-Comendite	
	Od-P3	Max. Th: 2 m. Massive, poorly sorted coarse to fine pumice lapilli breccia	Tephra fall	80% microvesicular & 1% tube pumice ≤5% free crystals (Fs, Ang/Px/Amp & Fe-Ti oxides) ≤3% lithics (hydr. altered lava, glassy obsidian & ignimbrite) <10% obsidian	60% vesicles No phenocrysts Glassy groundmass	Pantellerite-Comendite	
	Od-P4	Max. Th: 3 m. Cm-scale bedded, each bed set is normally graded pumice lapilli	Tephra fall; PDC	60-80% microvesicular & ≤1% tube pumice 10-20% free crystals (Fs,	55-65% vesicles ≤3%	Pantellerite-Comendite	4.7

	breccia underlain by a lithic-rich poorly sorted ash horizon		Ang, Amp, Px & Fe-Ti oxides) ≤25% lithics (hydr. altered lava, glassy obsidian & ignimbrite)	phenocrysts (Kfs, Cpx, Amp, Ang) Glassy to microlite-poor groundmass		
Od-P5	Max. Th: 3.5 m. Massive and poorly-sorted pumice lapilli breccia with occasional distinct bigger clasts (3.5 cm)	Tephra fall	60-70% microvesicular & ≤1% tube pumice 5-35% free crystals (Fs/Qtz, Ang/Px/Amp & Fe-Ti oxides) ≤3% lithics (hydr. altered lava & glassy obsidian) <25% obsidian		Pantellerite-Comendite	4.6
Od-P6	Max. Th: 90 cm. Main unit is massive poorly sorted pumice lapilli breccia. Its top and bottom are marked by thin ash beds (10-20 cm)	Tephra fall	95% microvesicular pumice 5% lithics (lava & glassy obsidian)		Pantellerite-Comendite	
Od-P7	Max. Th: 16 m. Interbedded horizons of coarse ash and rounded fine pumice lapilli, lenticular bedding, well sorted within each bed but deposit is poorly sorted overall	PDC	70% microvesicular pumice <25% free crystals (Fs/Qtz & Fe-Ti oxides) 1% lithics (hydr. altered lava, glassy obsidian & ignimbrite) <5% obsidian		Pantellerite-Comendite	
Od-P8	Max. Th: 1.85 m. Well-sorted coarse pumice lapilli breccia with subtle normal grading	Tephra fall	90% microvesicular & 1% expanded pumice 5% lithics (lava, glassy		Pantellerite-Comendite	

				obsidian & ignimbrite)			
Bora	**Bo-P1**	Max. Th: 1 m. Dm-scale crudely bedded, well-sorted pumice lapilli breccia; top few centimetres shows interbedding of coarse ash and pumice lapilli	Tephra fall	80% microvesicular, 5% expanded & 1% tube pumice <10% free crystals (Fs/Qtz & Fe-Ti oxides) 5% obsidian and lithics (lava, glassy obsidian & ignimbrite)		Pantellerite-Comendite	
	Bo-P2	Max. Th: 2.5 m. Cm-scale bedded, well-sorted pumice lapilli breccia with occasional pumice bombs (15 cm)	Tephra fall	60% microvesicular pumice ≤15% free crystals (Fs/Qtz & Fe-Ti oxides) <8% (hydr. altered lava, glassy obsidian & ignimbrite) 15% obsidian	60% vesicles No phenocrysts Glassy groundmass	Pantellerite-Comendite	4.3
	Bo-P3	Max. Th: >3 m. Massive, poorly to well-sorted coarse pumice lapilli breccia	Tephra fall	80% microvesicular, 5% expanded & 3% tube pumice 5% free crystals (Fs, Ang, Px & Fe-Ti oxides) ≤1% lithics (altered lava, glassy obsidian) 5% obsidian	45% vesicles <0.5% phenocrysts (Kfs & Opx) Microlite-poor groundmass	Pantellerite	4.2
Werdi	**Wd-P1**	Max. Th: >15 m. Cm-scale bedded, poorly sorted, coarse ash to medium sized bluish-grey pumice lapilli breccia	Tephra fall	83% microvesicular pumice 5% free crystals (Fs/Qtz, Ang/Px/Amp) 10% lithics (hydr. altered		Pantellerite-Comendite	4.6

				lava & crystal-rich obsidian)			
	Wd-P2	Max. Th: 35 cm. Massive, well-sorted, bluish-grey pumice lapilli breccia	Tephra fall	70% microvesicular pumice 20% free crystals (Fs, Ang & Fe-Ti oxides) <5% lithics (hydr. altered lava, glassy obsidian & ignimbrite) <5% obsidian	50% vesicles 1% phenocrysts (Kfs & Ang) Glassy groundmass	Pantellerite-Comendite	4.4
	Wd-P3	Max. Th: 2.1 m. Massive, poorly sorted, bluish-grey coarse pumice lapilli breccia	Tephra fall	<85% microvesicular pumice <10% free crystals (Fs/Qtz, Ang/Px/Amp) <10% lithics (hydr. altered lava, glassy obsidian & ignimbrite)		Pantellerite-Comendite	
Tullu Moye	**TM-P1**	Max. Th: 3 m. Massive, poorly sorted, white pumice lapilli breccia	Tephra fall	80-85% microvesicular, ≤2% expanded & <5% tube pumice ≤10% free crystals (Fs/Qtz, Px/Amp & Fe-Ti oxides) <10% lithics (hydr. altered lava & glassy obsidian)		Comendite	
	TM-P2	Max. Th: 2 m. Massive, poorly sorted, white pumice lapilli	Tephra fall	70-100% microvesicular, ≤1% expanded and ≤1%	60% vesicles 2%	Comendite	2.8

breccia containing occasional pumice bombs (15 cm)	tube pumice ≤20% free crystals (Fs, Px/Amp & Fe-Ti oxides) <3% (hydr. altered lava & glassy obsidian) <5% glassy obsidian	phenocrysts (Kfs, Cpx, Amp & Fe-Ti oxide) Glassy groundmass

Table 3

Group	**Suke**	**Meki**					**Baricha**				
Unit			**Ba-P1**	**Ba-P2**	**Ba-P3**	**Ba-P4**	**Ba-P5**	**Ba-P6**	**Ba-P7**	**Ba-P8**	**Ba-P9**
Sample (MER)	253-1D	149B	147-4F	205-2E	205-2C	147-2F	147-2A	147-1E	205-1B	147-1C	147-1A
Major	n=27	n=30	n=21	n=26	n=26	n=30	n=29	n=24	n=24	n=29	n=12
Trace	N=14	N=15	N=14	N=15	N=10	N=9	N=11	N=15	N=14		N=11
SiO_2	73.92(0.6)	74.08(0.3)	73.65(0.2)	73.91(0.6)	73.36(1.2)	74.03(0.2)	74.54(0.3)	74.01(0.4)	73.12(1.0)	73.75(0.3)	73.97(0.2)
TiO_2	0.36(0.1)	0.33(0.0)	0.22(0.1)	0.22(0.0)	0.22(0.0)	0.19(0.0)	0.23(0.0)	0.18(0.0)	0.21(0.0)	0.20(0.0)	0.21(0.0)
Al_2O_3	9.83(0.4)	8.72(0.1)	8.51(0.2)	9.04(0.2)	8.45(0.4)	8.57(0.1)	8.94(0.1)	8.74(0.4)	8.43(0.1)	8.45(0.1)	8.61(0.1)
FeO	5.65(0.3)	6.10(0.2)	6.51(0.2)	5.80(0.1)	6.12(0.4)	6.30(0.2)	5.77(0.2)	6.08(0.3)	6.25(0.3)	6.36(0.2)	6.21(0.2)
MnO	0.21(0.0)	0.23(0.0)	0.28(0.1)	0.24(0.0)	0.23(0.0)	0.27(0.1)	0.22(0.0)	0.23(0.0)	0.24(0.0)	0.27(0.0)	0.23(0.0)
MgO	0.01(0.0)	0.01(0.0)	0.01(0.0)	0.02(0.0)	0.01(0.0)	0.01(0.0)	0.01(0.0)	0.01(0.0)	0.00(0.0)	0.01(0.0)	0.01(0.0)
CaO	0.28(0.0)	0.23(0.0)	0.21(0.0)	0.20(0.0)	0.17(0.0)	0.18(0.0)	0.20(0.0)	0.17(0.0)	0.16(0.0)	0.16(0.0)	0.17(0.0)
Na_2O	4.97(0.7)	5.87(0.2)	6.22(0.2)	6.0(0.7)	7.00(1.5)	6.0(0.2)	5.62(0.1)	6.08(0.3)	7.14(1.2)	6.34(0.2)	6.17(0.2)
K_2O	4.74(0.3)	4.4(0.1)	4.39(0.1)	4.55(0.1)	4.43(0.2)	4.45(0.1)	4.47(0.1)	4.49(0.2)	4.43(0.1)	4.45(0.1)	4.42(0.1)
Rb	118	129	187	151	198	217	200	250	282		284
Sr	11	2	4	4	3	3	3	3	8		7
Y	100	100	154	119	168	176	167	200	220		207
Zr	1105	876	1443	1116	1653	1597	1664	2018	2240		2219
Nb	149	138	225	169	246	266	255	313	318		315

Cs	1	2	2	2	2	3	2	3	4		4
Ba	46	19	23	21	26	20	23	24	51		46
La	114	112	170	134	187	188	180	216	255		239
Ce	246	225	344	273	383	390	364	452	519		488
Nd	107	101	151	119	159	179	157	190	217		195
Sm	23	20	32	25	33	34	32	38	42		39
Eu	3	3	4	3	3	3	3	3	4		4
Gd	19	19	28	21	27	31	29	36	37		36
Dy	20	19	31	22	29	34	31	37	40		39
Yb	12	11	16	12	17	19	18	22	23		24
Hf	25	21	36	26	34	40	38	47	52		53
Ta	10	8	15	10	13	16	15	18	20		20
Th	20	17	27	21	28	31	29	35	42		40
U	4	4	7	5	6	8	7	9	11		10

Table 3 continued

Group		**Werdi**					**Oda**				
Unit	**Wd-P1**	**Wd-P2**	**Wd-P3**	**Od-P1**	**Od-P2**	**Od- P3**	**Od-P4**	**Od-P5**	**Od-P6**	**Od-P7**	**Od-P8**
Sample (MER)	368B n=18	155B n=28	155A n=23	336I n=19	336H n=17	336G n=28	336F n=18	336D n=14	336C n=18	330B n=16	336A n=19
SiO_2	74.79(0.6)	74.76(0.9)	74.03(1.1)	74.18(0.4)	74.11(0.4)	74.34(0.3)	75.11(0.4)	75.24(0.4)	74.90(0.4)	74.27(0.6)	75.14(0.5)
TiO_2	0.24(0.0)	0.31(0.0)	0.37(0.1)	0.34(0.0)	0.35(0.0)	0.35(0.0)	0.33(0.0)	0.31(0.0)	0.34(0.0)	0.24(0.0)	0.34(0.0)
Al_2O_3	8.94(0.2)	9.57(0.1)	8.82(0.2)	10.60(0.3)	10.58(0.2)	10.49(0.3)	9.72(0.3)	9.20(0.3)	9.30(0.3)	8.34(0.2)	9.42(0.1)
FeO	5.93(0.2)	5.23(0.3)	6.29(0.3)	4.71(0.1)	4.82(0.1)	4.62(0.2)	4.96(0.1)	5.23(0.1)	5.29(0.1)	6.35(0.7)	5.00(0.5)
MnO	0.23(0.0)	0.20(0.0)	0.24(0.1)	0.19(0.0)	0.19(0.0)	0.19(0.0)	0.19(0.0)	0.21(0.0)	0.21(0.0)	0.28(0.0)	0.21(0.0)
MgO	0.02(0.0)	0.01(0.0)	0.01(0.0)	0.02(0.0)	0.01(0.0)	0.01(0.0)	0.01(0.0)	0.01(0.0)	0.01(0.0)	0.01(0.0)	0.01(0.0)
CaO	0.2(0.0)	0.24(0.0)	0.28(0.1)	0.29(0.0)	0.30(0.0)	0.32(0.0)	0.24(0.0)	0.21(0.0)	0.22(0.0)	0.21(0.0)	0.23(0.0)
Na_2O	4.90(0.8)	5.04(0.9)	5.53(1.0)	5.08(0.2)	5.02(0.2)	4.99(0.4)	4.90(0.2)	5.16(0.1)	5.24(0.2)	5.79(0.3)	5.11(0.2)

K_2O	4.76(0.3)	4.61(0.4)	4.42(0.2)	4.59(0.2)	4.60(0.2)	4.67(0.2)	4.53(0.2)	4.44(0.1)	4.48(0.2)	4.51(0.1)	4.52(0.2)

Table 3 continued

Group		Bora		Tullu Moye	
Unit	**Bo-P1**	**Bo-P2**	**Bo-P3**	**TM-P1**	**TM-P2**
Sample (MER)	231D	231B	230A	152A	152B
	n=28	n=30	n=28	n=24	n=24
	N=	N=15		N=12	N=13
SiO_2	74.08(0.8)	74.65(0.2)	75.40(1.0)	72.06(0.2)	71.74(0.2)
TiO_2	0.34(0.0)	0.32(0.0)	0.20(0.0)	0.24(0.0)	0.30(0.0)
Al_2O_3	9.46(0.2)	9.36(0.1)	8.43(0.4)	13.28(0.1)	14.60(0.1)
FeO	5.43(0.4)	5.18(0.1)	6.22(0.2)	3.17(0.2)	1.89(0.1)
MnO	0.21(0.1)	0.19(0.0)	0.24(0.0)	0.15(0.0)	0.07(0.0)
MgO	0.01(0.0)	0.01(0.0)	0.01(0.0)	0.08(0.0)	0.24(0.0)
CaO	0.24(0.0)	0.22(0.0)	0.17(0.0)	0.41(0.0)	0.80(0.0)
Na_2O	5.74(0.3)	5.64(0.1)	5.37(0.9)	5.85(0.2)	4.93(0.2)
K_2O	4.48(0.1)	4.41(0.1)	3.94(0.4)	4.74(0.1)	5.37(0.1)
Rb	159	147		126	171
Sr	1	1		9	54
Y	105	98		66	24
Zr	984	977		766	415
Nb	166	150		112	66
Cs	2	2		1	2
Ba	28	25		401	562
La	120	112		85	60
Ce	254	235		172	103
Nd	109	101		72	31
Sm	21	20		13	5

Eu	3	3		2	1
Gd	18	18		12	4
Dy	19	18		12	4
Yb	11	11		8	3
Hf	24	22		18	10
Ta	10	9		7	5
Th	21	20		17	24
U	5	5		4	6